Charles University in Prague
Faculty of Mathematics and Physics

DIPLOMA THESIS

Mária Šoltésová

Experimental Investigation of Selected Supramolecular Systems by NMR Spectroscopy

Department of Low Temperature Physics

I would like to thank my supervisor, RNDr. Jan Lang, Ph.D., for his patience, continuous support and help during all the period of my work on the thesis. I am also grateful to Prof. Jozef Kowalewski, who supervised my work during my stay in Stockholm, for his support and guidance.

Prohlašuji, že jsem svou diplomovou práci napsala samostatně a výhradně s použitím citovaných pramenů. Souhlasím se zapůjčováním práce.

I hereby confirm that the diploma thesis submitted is entirely my own work and all other sources used are cited appropriately. I agree with lending of the thesis.

Prague, 14$^{\text{th}}$ August 2009 Mária Šoltésová

Contents

Abstract

Title: *Experimental Investigation of Selected Supramolecular Systems by NMR Spectroscopy*
Author: *Mária Šoltésová*
Department: *Department of Low Temperature Physics*
Supervisor: *RNDr. Jan Lang, Ph.D.*
Supervisor's e-mail address: *Jan.Lang@mff.cuni.cz*

Abstract: The thesis describes investigation of two selected supramolecular systems by means of NMR spectroscopy and hydrodynamic calculations. The first system studied was inclusion complex of cryptophane-C with chloroform. Initially, the kinetics of complexation was determined. The measurements of longitudinal relaxation and heteronuclear Overhauser enhancement on carbon-13 nuclei revealed very large motional coupling between the host and the molecular guest bound inside the cavity. Hydrogen bonded clusters of ethanol in a non-polar solvent were the second system addressed. The diffusion coefficients of ethanol were measured in a broad temperature range ($180-330$ K) by means of NMR spectroscopy. The average cluster sizes dependent upon experimental conditions were determined. At low temperature (around 180 K), the cluster sizes vary from hexamer (0.16 M sample) to octamer or larger structures (1.4 M sample). On the other hand, the average cluster size at ambient temperature corresponds to trimer (1.4 M), pure monomer occurs in the less concentrated sample above 308 K. Experimental results for monomer are in excellent agreement with the calculated values.

Keywords: NMR, cryptophane, host-guest complex, ethanol, molecular cluster, translational diffusion

Abstrakt

Název práce: *Experimentální studium vybraných supramolekulárních systémů pomocí NMR spektroskopie*
Autor: *Mária Šoltésová*
Katedra (ústav): *Katedra fyziky nízkých teplot*
Vedoucí diplomové práce: *RNDr. Jan Lang, Ph.D.*
e-mail vedoucího: *Jan.Lang@mff.cuni.cz*

Abstrakt: Práca popisuje štúdium dvoch vybraných supramolekulárnych systémov pomocou NMR spektroskopie a hydrodynamických výpočtov. Prvým študovaným systémom bol inklúzny komplex kryptofanu-C s chloroformom. Bola stanovená kinetika komplexácie a za pomoci meraní pozdĺžnej relaxačnej doby a heteronukleárneho Overhauserovho javu bola zistená veľmi vysoká pohybová väzba medzi hostiteľom a molekulárnym hosťom viazaným v kavite. Druhým študovaným systémom boli vodíkovo viazané klastre etanolu v nepolárnom rozpúšťadle. Pomocou NMR spektroskopie boli zmerané difúzne koeficienty etanolu v širokom rozsahu teplôt (180 – 330 K). Porovnaním s hydrodynamickým výpočtom pre štruktúry klastrov získaných pomocou kvantovo-chemických výpočtov bola stanovená priemerná veľkosť klastrov v závislosti na experimentálnych podmienkach. Pri nízkej teplote (180 K) sa priemerná veľkosť klastrov pohybuje od hexaméru (0,16 M vzorka) po oktamér, prípadne väčšie štruktúry (1,4 M vzorka). Priemerná veľkosť klastrov pri 298 K v 1,4 mM vzorke zodpovedá triméru a v 0,16 M vzorke je počínajúc od teploty 308 K prítomný monomér. Experimentálne hodnoty pre monomér sú v výbornom súhlase s vypočítanými hodnotami.

Kľúčová slová: NMR, kryptofan, host-guest komplex, etanol, molekulárny klaster, translačná difúzia

Part I

Introduction and Theory

Chapter 1

Introduction

1.1 Non-Covalent Interactions and Supramolecular Systems

Molecular structure of chemical and biological species is primarily determined by covalent bonding. Non-covalent interactions, albeit being generally substantially weaker, provide a subtle mechanism that often controls molecular overall and internal mobility. Their energetic contribution is responsible for adoption of a certain conformation in flexible molecular systems. Non-covalent interactions thus often control chemical reactions, which is of primary importance in biological systems. Current supramolecular chemistry attempts very successfully to utilize these week interactions to perform new unprecedented chemical reactions and produce molecular systems with novel properties and many new applications. Non-covalent interactions are also responsible for macroscopic thermodynamic properties of liquids consisting of species capable of hydrogen bonding.

Due to inherent connection between the non-covalent interactions and molecular mobility and flexibility, nuclear magnetic resonance (NMR) appears to be experimental method of choice to assess properties of the supramolecular systems. NMR spectroscopy is able to provide detailed information about the structure as well as the dynamics of the system. As dynamics may appear in many different time-scales, NMR offers plenty of methodologies to characterize all motions occurring from picoseconds to any longer time-scales up to days.

This work is dealing with two supramolecular systems: the inclusion complex of cryptophane-C with chloroform and hydrogen bonded molecular clusters of ethanol. The similarity of the two systems lies in the fact that week interactions play essential role in their microscopic structures as well as dynamics. The investigation of the host-guest complex of cryptophane-C and chloroform was completed during the semester stay at the Department of Physical, Inorganic and Structural Chemistry, Stockholm University under supervision of Prof. Jozef Kowalewski. The alcohol clusters study was accomplished at the Department of Low Temperature Physics, Charles University in Prague under supervision of RNDr. Jan Lang, Ph.D.

1.2   Motivation

Cryptophanes are a ball shaped molecules with pronounced complexation affinity towards neutral guests [1]. Cryptophanes are recognized as one of important building blocks of current supramolecular chemistry. So far, cryptophane molecules have been used mainly to investigate the binding properties of a variety of guests and to model guest binding in more complex biological molecules. More recently, there is increasing interest in these molecules, particularly to physical chemists and spectroscopists. A main interest concerns the physical behavior of the guest molecule in the confined space of the molecular cavity of the cryptophanes compared to that of the guest in the solvent. Cryptophanes are indeed considered among the first molecular hosts possessing selective encapsulation properties, thus enabling to isolate a substrate from the neighboring environment.

The main goal of investigation of cryptophane-C – chloroform complex was determination of binding kinetics and especially determination of the degree of motional coupling between the host and the guest inside of the host's cavity. The nature of motional coupling may reveal details concerning the week interactions between host and the guest.

Other interesting example of supramolecular complexes are hydrogen-bonded structures of ethanol molecules in solution – molecular clusters. Although hydrogen bonding in liquids was in interest among the physicists and chemists for more than fifty years, no consistent theory involving the microscopic properties of the clusters as well as the thermodynamic of their formation has been developed. The knowledge that can be found in literature is sometimes inconsistent and fragmentary. Most works investigating clusters in liquids by means of NMR concerns the temperature dependence of hydroxyl proton chemical shift. We have applied a novel approach, which combines NMR diffusion measurements with quantum chemical and hydrodynamic calculations.

Our motivation to study ethanol-ethanol interaction originated in polymer physics. Binary solutions of ethanol with other solvents can be used for collapsing hydrogels [2]. Hydrogels are polymers capable of the coil-globule phase transition (collapse) induced by the change of physical properties, e.g. temperature or solvent composition. At this phase transition, solvent is rapidly excluded from the polymeric structure and polymer forms tight globules. In order to understand the thermodynamics of the coil-globule phase transition, it is necessary to account for the contribution of solvent-solvent interaction, which is often neglected with respect to solute-solute and solute-solvent free energy contributions. We believe that methodology of determination of average size of the present clusters is a contribution to this effort.

1.3   Organization of the Thesis

The thesis begins with the common theoretical introduction dealing with the basics of nuclear magnetic resonance and nuclear spin relaxation. This part contains also introduction to translational diffusion and chemical exchange,

which are important in this study. Then, the part concerning NMR experimental techniques follows. Pulse sequences of 1D and 2D measurements used in this work and their properties are described there.

The two supramolecular systems studies are described in the following parts of the thesis. Each of them contains experimental parts describing compositions of sample and details of experiments carried out, presentation and discussion of the results and summary of major achievements on the both systems.

The strategy of investigation of the ethanol clusters was as follows: Firstly, calibration measurements of tetramethylsilane (TMS) diffusion in non-deuterated hexane were carried out. In the next step, the parameters of HydroNMR program were adjusted so that calculations for TMS correspond to the experimental value. Subsequently, the diffusion of the theoretically calculated (density functional theory) cluster structures [3] was simulated by HydroNMR with the optimized settings. Finally, the temperature dependence of diffusion coefficients of ethanol in deuterated hexane was acquired. As a main result of this project, temperature dependence of the average cluster sizes based on the comparison of calculated and experimental diffusion data is presented.

The investigation of inclusion complex of cryptophane-C and chloroform involved proton and carbon-13 spectra assignment by means of homo- and hetoronuclear 2D experiments. Then, kinetics of the host-guest complex formation was determined. In the last step, carbon-13 relaxation parameters for both the host and the guest were measured and discussed in terms of mutual motional coupling.

Chapter 2

Theory

2.1 Basic Principles of NMR

2.1.1 Single Spin in the Magnetic Field

Nuclear magnetic resonance (NMR) is a phenomenon at which resonating behaviour of nuclei with non-zero spin angular momentum $\hat{\boldsymbol{I}}$ and non-zero nuclear magnetic moment $\hat{\boldsymbol{\mu}}$ in external magnetic field occurs. The spin angular momentum is simply related to the nuclear magnetic moment as

$$\hat{\boldsymbol{\mu}} = \gamma \hbar \hat{\boldsymbol{I}}, \tag{2.1}$$

where the quantity γ is called *magnetogyric ratio* and $\hbar$ is reduced Planck constant.

When a nuclear spin is placed in an external static magnetic field, $\boldsymbol{B}_0$, the field interacts with the magnetic moment $\hat{\boldsymbol{\mu}}$. This interaction is called *Zeeman interaction* and it is described by Zeeman Hamiltonian

$$\hat{H}_0 = -\hat{\boldsymbol{\mu}} \cdot \boldsymbol{B}_0 = -\gamma \hbar \hat{\boldsymbol{I}} \cdot \boldsymbol{B}_0. \tag{2.2}$$

The static external magnetic field in NMR is always assumed to define the laboratory-frame z-axis. In this convention $\boldsymbol{B}_0 = (0, 0, B_0)$, which simplifies Equation 2.2 to

$$\hat{H}_0 = -\mu_z B_0 = -\gamma \hbar I_z B_0, \tag{2.3}$$

where I_z is the z-component of the nuclear spin operator.

According to the solution of the Schrödinger equation with Hamiltonian 2.3, the energy of the spin splits to $2I + 1$ equidistant energy levels, called Zeeman multiplet. The eigenvalues of Zeeman Hamiltonian

$$E_m = -\gamma \hbar B_0 m \tag{2.4}$$

are the energies of the levels for particular magnetic quantum number m. The distance ΔE of the levels is

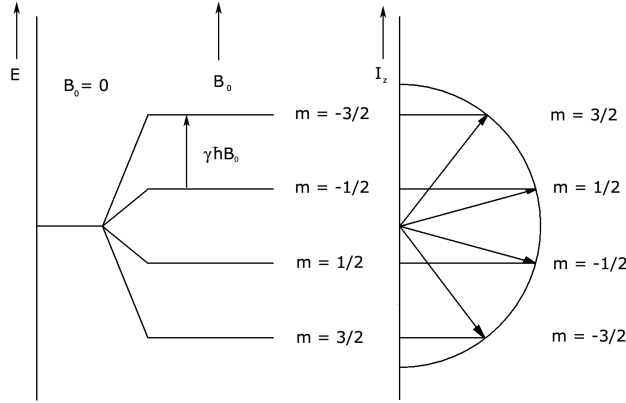$$\Delta E = |\gamma| \hbar B_0. \tag{2.5}$$

Figure 2.1: Zeeman multiplet for $I = 3/2$.

Different energy levels corresponds to the different orientation of the magnetic moment $\hat{\boldsymbol{\mu}}$ with respect to the external magnetic field $\boldsymbol{B}_0$. Figure 2.1 from [4] shows an example of Zeeman multiplet for $I = 3/2$ and $\gamma > 0$ together with corresponding orientations of the magnetic moment. For $I = 1/2$, two energy levels would be present.

Quantum mechanics does not require the system to be in a specific eigenstate of the Hamiltonian. The system can also exist in a superposition state, i.e., a superposition of the energy eigenvalues.

Let us consider, in addition to the static field $\boldsymbol{B}_0$, also time-dependent field $\boldsymbol{B}_1(t)$ with constant amplitude rotating with constant angular frequency $\boldsymbol{\omega}$ in xy-plane. The overall magnetic field in this situation will be

$$\boldsymbol{B} = B_1 \left(\boldsymbol{i} \cos \omega_z t + \boldsymbol{j} \sin \omega_z t \right) + \boldsymbol{k} B_0, \tag{2.6}$$

where $\boldsymbol{i}$, $\boldsymbol{j}$, $\boldsymbol{k}$ are unit vectors in x, y, z directions. The Hamiltonian of the interaction between the magnetic field and the nuclear spin has a form

$$\hat{H} = \hat{H}_0 + \hat{H}_1(t). \tag{2.7}$$

where the first term, $\hat{H}_0$, is given according to Equation 2.3 and the second term, $\hat{H}_1(t)$, describing interaction with the field $B_1(t)$, can be expressed as follows

$$\hat{H}_1(t) = -\hat{\boldsymbol{\mu}} \cdot \boldsymbol{B}_1(t) = -\gamma \hbar B_1 \left(I_x \cos \omega_z t + I_y \sin \omega_z t \right) =$$
$$= -\frac{B_1}{2} \gamma \hbar \left(e^{i\omega_x t} I_- + e^{-i\omega_z t} I_+ \right). \tag{2.8}$$

Operators I_+ a I_-, so called raising and lowering operators, are defined as

$$I_{\pm} = I_x \pm i I_y \tag{2.9}$$

and by acting on eigenfunction of I_z operator lower or rise the value of magnetic quantum number m by one, respectively.

13

Considering that $B_1 \ll B_0$, the influence of time-dependent operator $H_1(t)$ can be studied by means of the time-dependent perturbation theory. According to this theory, small perturbation can induce transitions between the stationary states of unperturbed system. The transition probability $P_{m',m}$ between the states characterized by quantum numbers m' and m is directly proportional to the square root of the matrix element of the perturbation Hamiltonian (see for example [4])

$$P_{m',m} \sim \left| \langle m' | H_1 | m \rangle \right|^2. \tag{2.10}$$

From the form of Hamiltonian 2.8 containing operators I_+ a I_-, it is obvious that the only non-zero matrix elements will be those with $m' = m \pm 1$. The magnetic field $\boldsymbol{B}_1$ will therefore induce only transitions between the neighbouring energy levels of Zeeman multiplet. Due to the symmetry of the matrix elements $\langle m' | H_1 | m \rangle$, transitions to the lower or higher energy level are equally probable.

The transition induced by the field $\boldsymbol{B}_1$ is connected to the absorption or emission of an energy quantum ΔE (Eq. 2.5). We can introduce *Larmor frequency* $\boldsymbol{\omega}_0$ as

$$\boldsymbol{\omega}_0 = -\gamma \boldsymbol{B}_0 \tag{2.11}$$

and then Equation 2.5 becomes

$$\Delta E = \hbar \omega_0, \tag{2.12}$$

which gives a condition for the frequency of magnetic field $\boldsymbol{B}_1$ necessary for induction of transition between the neighbouring levels of Zeeman multiplet by this field.

2.1.2   Bloch Equations

So far, only properties of single spin were considered. However, in NMR experiments, behaviour of macroscopic samples of spins is important. A theoretical tool we need to use is that of an *ensemble* of spins – a large collection of identical and independent systems. For simplicity, we deal here with an ensemble of spin-1/2 particles, interacting with the magnetic field through Zeeman interaction but not interacting with each other.

An ensemble of non-interacting nuclear spins at the thermal equilibrium can be represented by a *magnetization vector* – an ensemble averaged nuclear magnetic moment, $\boldsymbol{M}$, oriented along the direction of the external magnetic field. As we shall see later, the spins interact with each other, however, the simplification of non-interacting spins is reasonable approach of spin behaviour in isotropic liquids at particular cases.

The magnetization vector is a macroscopic quantity and its motion can be described using classical physics. To describe an NMR experiment, we need to consider the presence of a static magnetic field $\boldsymbol{B}_0$, as well as the time-dependent magnetic field $\boldsymbol{B}_1(t)$.

A very simple model describing motion of magnetization vector in the magnetic field is described by *Bloch equations*, which can be written in following

form:

$$\frac{\mathrm{d}M_x}{\mathrm{d}t} = \gamma\left(\boldsymbol{M} \times \boldsymbol{B}\right)_x - \frac{M_x}{T_2} \tag{2.13}$$

$$\frac{\mathrm{d}M_y}{\mathrm{d}t} = \gamma\left(\boldsymbol{M} \times \boldsymbol{B}\right)_y - \frac{M_y}{T_2} \tag{2.14}$$

$$\frac{\mathrm{d}M_z}{\mathrm{d}t} = \gamma\left(\boldsymbol{M} \times \boldsymbol{B}\right)_z - \frac{M_z - M_0}{T_1}. \tag{2.15}$$

Bloch equations are phenomenological, i.e., they aim at a simple description of the observed NMR phenomenon, without requirements of a strict derivation. Besides the *coherent* motion or preccesion around the effective fields, they take into consideration also the *incoherent* motion or *nuclear spin relaxation.*

Equation 2.13 describes the time variation of the *longitudinal* (along the external field) component of magnetization vector. The equation predicts the magnetization component along $\boldsymbol{B}_0$ to relax exponentially to its equilibrium value, M_0. The time constant for that process is called *spin-lattice* or *longitudinal* relaxation time and is denoted T_1. Equations 2.14 and 2.15 describe the motion of the transverse components of magnetization vector. The first part of the expression corresponds to the coherent motion of $\boldsymbol{M}$ in the rotating frame. The second part introduces the concept of the *transverse*, or *spin-spin relaxation time*, T_2, describing the exponential decay of the xy-magnetization to its equilibrium value of zero.

2.2 NMR Interactions

Besides the already mentioned Zeeman interaction between the nuclear spins and the external magnetic field, nuclear spins also interact with each other. This fact reflects in NMR spectra as well as in relaxation.

2.2.1 Chemical Shielding

Electrons present within the molecule influence the nuclear spin, therefore the local field $\boldsymbol{B}_{loc}$ experienced by the nucleus is not equal to the external field of the NMR magnet $\boldsymbol{B}_0$. The external field induces electron currents that cause small perturbation proportional to the external field. This phenomenon is called *chemical shielding.* The local field is given by

$$\boldsymbol{B}_{loc} = \boldsymbol{B}_0(1 - \overleftrightarrow{\boldsymbol{\sigma}}) \tag{2.16}$$

and the chemical shielding Hamiltonian for a single spin I in the Cartesian coordinates is

$$\hat{H}_{CS} = \gamma_I \hat{\boldsymbol{I}} \cdot \overleftrightarrow{\boldsymbol{\sigma}} \cdot \boldsymbol{B}_0, \tag{2.17}$$

where the symbol $\overleftrightarrow{\boldsymbol{\sigma}}$ denotes the *shielding tensor.* The shielding tensor is a property of a particular nucleus in a molecule or a crystal and therefore it is naturally expressed in the molecular coordinate system. The shielding is in

general anisotropic, meaning that it is orientation dependent. The necessity of describing the phenomenon of shielding with a shielding tensor, rather than a simpler object such a scalar, reflects the fact that the induced field does not have to be parallel to the external field $\boldsymbol{B}_0$.

In isotropic liquids, due to the averaging caused by thermal motion, only isotropic component of the chemical shielding tensor, σ_{iso}, is important:

$$\sigma_{iso} = \frac{1}{3}\left(\sigma_{11} + \sigma_{22} + \sigma_{33}\right). \tag{2.18}$$

The absolute magnitude of the chemical shielding is in general dependent on the magnitude of the external magnetic field $\boldsymbol{B}_0$. To allow more convenient comparison of the different experimental results, relative scale independent on the measuring apparatus was established. Standard molecules having Larmor frequency ω_{st} were chosen for common magnetically active nuclei and quantity *chemical shift* denoted δ given in ppm (parts per million) was defined as

$$\delta^{iso}[\text{ppm}] = \frac{\omega_0 - \omega_{st}}{\omega_{st}}10^6 = \frac{\sigma_{st} - \sigma_{iso}}{1 - \sigma_{st}}10^6 \approx \left(\sigma_{st} - \sigma_{iso}\right)10^6, \tag{2.19}$$

where ω_0 is Larmor frequency of the measured substance. For carbon and proton spectra, standard molecule is tetramethylsilane (TMS), $Si(CH_3)_4$.

2.2.2 Direct Dipole-Dipole Interaction

The direct dipole-dipole interaction is the strongest interaction for nuclei with the spin $I = 1/2$. It is the interaction between two nuclear magnetic moments or magnetic dipoles, $\boldsymbol{\mu}_1$ and $\boldsymbol{\mu}_2$, close to each other in space. Each of the magnetic dipoles generates generates around itself a local magnetic field and other dipoles react to this field. The local field generated by the dipole $\boldsymbol{\mu}_2$ at the point $\boldsymbol{r}$ can be expressed by

$$\boldsymbol{B}_{loc} = -\frac{\mu_0}{4\pi r^3}\left(\boldsymbol{\mu}_2 - 3\frac{\boldsymbol{\mu}_2\boldsymbol{r}}{r^2}\cdot\boldsymbol{r}\right) \tag{2.20}$$

where μ_0 is the permeability of vacuum, r is the distance from the origin and $\boldsymbol{r}$ is a vector with Cartesian components x, y, z. Having in mind that $\boldsymbol{\mu}_1 = \gamma_1\hbar\hat{\boldsymbol{I}}$ and $\boldsymbol{\mu}_2 = \gamma_2\hbar\hat{\boldsymbol{S}}$, the Hamiltonian of the dipole-dipole interaction for the two spins I and S can be written in a form

$$\hat{H}_{DD} = -\frac{\mu_0\gamma_I\gamma_S\hbar}{4\pi r^3}\left(3\hat{\boldsymbol{I}}\cdot\frac{\boldsymbol{r}\boldsymbol{r}}{r^2}\cdot\hat{\boldsymbol{S}} - \hat{\boldsymbol{I}}\cdot\hat{\boldsymbol{S}}\right) = b_{IS}\hat{\boldsymbol{I}}\cdot\overset{\leftrightarrow}{\boldsymbol{D}}\cdot\hat{\boldsymbol{S}}. \tag{2.21}$$

where $\overset{\leftrightarrow}{\boldsymbol{D}}$ is the *dipolar tensor*. If the distance between spins r is constant and equal to r_{IS}, then the quantity b_{IS} given by

$$b_{IS} = -\frac{\mu_0\gamma_I\gamma_S\hbar}{4\pi r_{IS}^3} \tag{2.22}$$

is also a constant, denoted as *dipole-dipole coupling constant*.

In case of isotropic liquids, the dipole-dipole interaction vanishes due to the molecular tumbling, which changes the orientation of IS-spin axis on a time scale that is very fast compared to the dipole-dipole couplings. This does not mean, however, that the dipole-dipole interaction cannot be effective as a relaxation mechanism.

2.2.3 Indirect Dipole-Dipole Coupling (J-Coupling)

Indirect dipole-dipole coupling, or J-coupling, is an indirect interaction between two spins mediated by bond electrons. While direct dipole-dipole coupling is averaged to zero in isotropic liquids, J-coupling influences spectra of liquid substances as well. The Hamiltonian of J-coupling for two spins I and S is

$$\hat{H}_J = 2\pi \hat{\boldsymbol{I}} \cdot \overset{\leftrightarrow}{\boldsymbol{J}} \cdot \hat{\boldsymbol{S}} \tag{2.23}$$

where $\overset{\leftrightarrow}{\boldsymbol{J}}$ is the *J-coupling Cartesian tensor*.

Two spins have measurable indirect dipole-dipole coupling only when they are connected to each other with small number of chemical bonds. That implies that J-coupling is mostly intramolecular, however, intermolecular examples of J-coupling can be also found, for instance when hydrogen bonds are involved.

J-coupling causes splitting of signals in spectra to multiplets. In case of interaction of two nuclei with the spin of 1/2, the spectral line is split into doublet. Splitting of spectral lines provides useful information about the chemical bonding in the studied sample.

2.2.4 Other Interactions

Besides above mentioned interactions, several other interactions may occur. One of them is for example spin-rotational interaction, which is interaction between nuclear spins and magnetic field generated by rotational motion of the molecule. This interaction is important only in gaseous state NMR or in samples with very small molecules. In isotropic liquids, this interaction is averaged to zero due to random fluctuations of molecular motion.

Apart from magnetic interactions, electron quadrupolar interaction may be also present. This interaction may be very strong for nuclei with spin higher than 1/2, but does not concern spin-1/2 nuclei.

2.3 Translational Diffusion

Molecules (or generally any particles) in liquid phase undergo Brownian motion which displaces them in space. This phenomenon is known as an *translational diffusion*, and its characteristics are reflected in the *diffusion coefficient D*. According to the Stokes-Einstein theory

$$D = \frac{k_B T}{f_T}, \tag{2.24}$$

where k_B is the Boltzman constant, T is the absolute temperature and f_T is the friction factor. For the special case of a spherical particle of hydrodynamic radius r_H in a solvent of viscosity η, the friction factor is given by

$$f_T = 6\pi\eta r_H. \tag{2.25}$$

Combining Equations 2.24 and 2.25, it is possible to express the hydrodynamic radius as

$$r_H = \frac{k_B T}{6\pi\eta D}.$$ (2.26)

Pulsed field gradient NMR spectroscopy can be used to measure translational diffusion of molecules. By use of a gradient, molecules can be spatially labeled, i.e. marked depending on their position in the sample tube. If we apply gradient of external magnetic field

$$\boldsymbol{G} = \frac{\partial B_z}{\partial x}\boldsymbol{i} + \frac{\partial B_z}{\partial y}\boldsymbol{j} + \frac{\partial B_z}{\partial z}\boldsymbol{k},$$ (2.27)

where $\boldsymbol{i}$, $\boldsymbol{j}$, $\boldsymbol{k}$ are unit vectors in x, y, z directions, the magnitude of magnetic field at the position $\boldsymbol{r}$ will be

$$B(\boldsymbol{r}) = B_0 + \boldsymbol{G} \cdot \boldsymbol{r}.$$ (2.28)

For measuring translational diffusion, it is sufficient that only z-gradient of magnitude $G = \boldsymbol{G} \cdot \boldsymbol{k}$ in the direction of the main field is considered. If, owing to this gradient, the magnetic field varies along the z-axis according to

$$B(z) = B_0 + G(z),$$ (2.29)

so does the Larmor frequency ω of the nuclei

$$\omega(z) = -\gamma\left[B_0 + G(z)\right].$$ (2.30)

The phase angle $\Phi(z)$ for each spin depends on position of the nuclei along the z-axis:

$$\Phi(z) = -\omega(z)\delta = -\gamma B(z)\delta,$$ (2.31)

where δ is the duration of the pulse gradient. Thus, the position of the nuclei along the z-axis is encoded according by their phase angle. If the nuclei moves after this encoding during the following delay Δ, their new position can be detected by a second gradient. The measured signal is the integral over the whole sample volume and the NMR signal intensity is attenuated depending on the delay Δ, the length δ and strength G of the gradient

$$I_{(2\tau,G)} = I_{(2\tau,0)}e^{-D\gamma^2 G^2 \delta^2(\Delta - \delta/3)},$$ (2.32)

where $I_{2\tau,G}$ is the intensity of the signal in time 2τ (in the maximum of the echo) with the gradient applied, $I_{2\tau,0}$ is the signal intensity in time 2τ without applied gradient, D is the diffusion coefficient, γ is the magnetogyric ratio and $\Delta - \delta/3$ is the diffusion time. By fitting Equation 2.32 to the Gaussian decaying function, it is possible to obtain the translational diffusion coefficient.

For specific pulse sequences used for diffusion measurements, see Section 3.3.

2.4   Hydrodynamic Simulations

For hydrodynamic simulations included in this work, program HydroNMR [5] was used. HydroNMR is a computer program intended for the calculation of basic hydrodynamic quantities and NMR relaxation of small, quasirigid macromolecules.
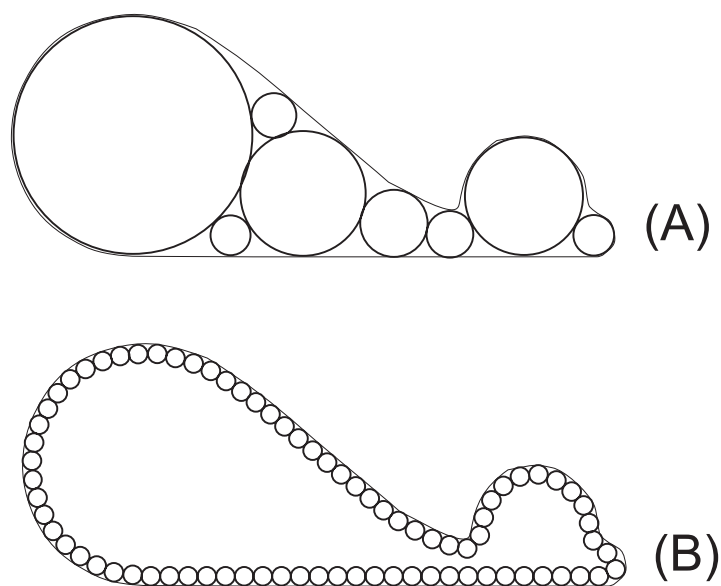
Figure 2.2: Two-dimensional analogies of the various model types. (A) A bead model in a strict sense, (B) Shell model [8].

2.4.1   Bead Models

The hydrodynamic properties of rigid particles can be calculated from models composed of spherical elements – beads. This approach is called *bead-modeling* [6, 7]. In general sense, bead model is any representation of a particle as an array of spherical friction elements. However, for any particle given, there are different strategies for building the hydrodynamic bead model. Sometimes the beads are few and of varying size (*bead model in the strict sense*), and other times there are many small beads filling the molecule as a whole (*filling model*) or just its surface (*shell model*). Schematic representation of different kinds of bead model is depicted in Figure 2.2.

In case of the HydroNMR program, the shell-model methodology is employed [6, 7, 9, 8]. Considering the fact that for a compact solid particle, the hydrodynamic friction occurs on its surface, one can use a model, in which the particle's surface is represented by a shell-like assemblage of many small, identical friction elements. The bead radius, σ, can be taken such that the neighbouring particles are tangent to each other. The limit of a continuous shell (smooth surface) is approached by increasing the number of elements, N_σ, while decreasing the size, and the properties calculated from the shell model will approach the properties of the particle being modeled.

2.4.2 Principles of Hydrodynamic Calculations in HydroNMR

The theory of the hydrodynamic calculations necessary for bead models, as introduced in [8], can be summarized as follows:

For a particle of arbitrary shape, the hydrodynamic resistance is expressed by means of a 6×6 resistance or friction tensor, Ξ. Similarly, the Brownian diffusivity is expressed by a 6×6 diffusion matrix, $\mathcal{D}$, which is related to Ξ through the generalized Einstein relationship

$$\mathcal{D} = k_B T \Xi^{-1}. \tag{2.33}$$

Friction tensor Ξ as well as diffusion matrix $\mathcal{D}$ can be partitioned in 3×3 blocks, which corresponds to translation (tt), rotation (rr) and translation-rotation coupling (tr), so that

$$\mathcal{D} = \begin{pmatrix} \boldsymbol{D}_{tt} & \boldsymbol{D}_{tr}{}^T \\ \boldsymbol{D}_{tr} & \boldsymbol{D}_{rr} \end{pmatrix} = k_B T \begin{pmatrix} \Xi_{tt} & \Xi_{tr}{}^T \\ \Xi_{tr} & \Xi_{rr} \end{pmatrix}^{-1}. \tag{2.34}$$

The superscript T indicates transcription. From the (tt) block, the translational diffusion D_t is given by

$$D_t = \frac{1}{3} \mathrm{Tr}(\boldsymbol{D}_{tt}) \tag{2.35}$$

and the friction coefficient f_t as

$$f_t = \frac{k_B T}{D_t}, \tag{2.36}$$

where Tr is the trace of the tensor.

The theory of hydrodynamic properties of bead models provides a procedure to calculate the components of Ξ. A key concept in bead model hydrodynamics is the hydrodynamic interaction effect. The frictional force experienced by a bead depends not only on its relative velocity and its frictional coefficient, but also on the frictional forces that act at all the other beads. From the Cartesian coordinates and radii of the N beads in the model, the 3×3 hydrodynamic interaction tensor between beads i and j, $\boldsymbol{T}_{ij}$, are calculated. This tensor was originally formulated by Oseen as

$$\boldsymbol{T}_{ij} = (8\pi\eta_0 R_{ij})^{-1} \left(\boldsymbol{I} + \boldsymbol{R}_{ij}\boldsymbol{R}_{ij}/R_{ij}^2 \right), \tag{2.37}$$

where $\boldsymbol{I}$ is the unit tensor $\boldsymbol{R}_{ij}$ is the distance vector between elements i and j. In the derivation of Equation 2.37, it was implicitly assumed that the size of the elements is much smaller than R_{ij}. Therefore, a new expression valid for interacting elements of equal size was derived

$$\boldsymbol{T}_{ij} = \frac{1}{6\pi\eta_0\sigma} \left(\left(1 - \frac{9}{32}\frac{R_{ij}}{\sigma} \right) \boldsymbol{I} + \frac{3}{32}\frac{\boldsymbol{R}_{ij}\boldsymbol{R}_{ij}}{R_{ij}\sigma} \right), \tag{2.38}$$

which was later generalized for elements of different radii σ_i a σ_j

$$\boldsymbol{T}_{ij} = (8\pi\eta_0 R_{ij})^{-1}\left(\boldsymbol{I} + \frac{\boldsymbol{R}_{ij}\boldsymbol{R}_{ij}}{R_{ij}^2} + \frac{\sigma_i^2 + \sigma_j^2}{R_{ij}^2}\left(\frac{1}{3}\boldsymbol{I} - \frac{\boldsymbol{R}_{ij}\boldsymbol{R}_{ij}}{R_{ij}^2}\right)\right). \qquad (2.39)$$

This equation is valid only if $R_{ij} \geq \sigma_i + \sigma_j$. Othervise, beads i a j overlap.

Now we define a $3N \times 3N$ supermatrix $\mathcal{B}$ composed of 3×3 blocks:

$$\boldsymbol{B}_{ij} = \boldsymbol{T}_{ij} \text{ ak } i \neq j, \qquad (2.40)$$

$$\boldsymbol{B}_{ij} = \frac{1}{\xi_i}\boldsymbol{I}, \qquad (2.41)$$

where

$$\xi_i = 6\pi\eta_0\sigma_i \qquad (2.42)$$

is the Stokes' law friction coefficient of bead i, with radius σ_i, η_0 being the viscosity of the solvent. This supermatrix is inverted to obtain a $3N \times 3N$ supermatrix

$$\mathcal{S} = \mathcal{B}^{-1}, \qquad (2.43)$$

that is partitioned in 3×3 blocks, $\boldsymbol{C}_{ij}$, which in turn gives the components of Ξ, particularly Ξ_{tt}, as

$$\Xi_{tt} = \sum_i \sum_j \boldsymbol{C}_{ij}. \qquad (2.44)$$

Summarizing, the computational route is as follows: from the Cartesian coordinates and the radii of beads, we calculate the $\boldsymbol{T}_{ij}$ tensors (Eq. 2.39) and build the $\mathcal{B}$ supermatrix (Eqs. 2.40, 2.41), which is inverted to obtain $\mathcal{S}$ (Eq. 2.43). The components of Ξ are calculated from Eq. 2.44. Then, Ξ is inverted to obtain $\mathcal{D}$, which is partitioned into four 3×3 blocks, from which the translational and rotational properties are calculated from Eqs. 2.35 and 2.36.

2.4.3   Input Parameters for HydroNMR

HydroNMR requires two input files to be supplied. The first one specifies primary data such as temperature, solvent density, etc., the second one is a PDB data file containing atomic coordinates of the molecule. According to the information contained within the structural file, HydroNMR creates *primary hydrodynamic model* for the given molecule. This model is constructed by simply replacing all the non-hydrogen atoms within the molecule with *atomic spheres* or *elements* having radius a. The primary hydrodynamic model is not used in the hydrodynamic calculation. Instead, a shell model composed of *minibeads* of radius σ is derived from it. Program runs several times for different σ and extrapolation to the shell model limit of $\sigma \to 0$ is carried out.

For this purpose, the following information has to be supplied in input file (as suggested by authors of HydroNMR in the user guide [10]):

- Parameter a – effective radius of the atomic elements, value of 3.2 Å is recommended for proteins.

- Parameter N_σ – number of values of the radius of minibeads. It must be grater than 2 (typically 5 to 8). The radius will range from σ_{min} to σ_{max}.

- Parameter σ_{min} – lowest value of the minibead radius σ.

- Parameter σ_{max} – highest value of the minibead radius σ.

The smaller the size of minibeads, the larger the number of them needed to cover the surface of the particle. The present version of the program works with a maximum of 2000 minibeads. The value of σ_{min} should not be too small to extend the number of 2000 minibeads and the value of σ_{max} should be taken such that the number of minibeads is not too small, suggested to be in the range 200-400.

2.5   Chemical Exchange

Chemical exchange in general is any process at which spins in the molecule changes their magnetic environment. This may be due to chemical reaction, isomerization, conformational changes, complexation of molecules, etc. These phenomenons reflects in NMR spectra and NMR relaxation. In our case, chemical exchange is caused by inclusion complex formation.

The complex formation between the guest (G) and the host (H) can be expressed by a chemical reaction (depicted in Figure 2.3)

$$H + G \underset{k_{-1}}{\overset{k_1}{\rightleftharpoons}} HG, \tag{2.45}$$

where k_1 and k_{-1} are the reaction rates of free-to-bound and bound-to-free reaction, respectively.

For the interpretation of NMR experiments, the effective chemical exchange rates are defined as

$$k_{FB} = k_1[H], \qquad k_{BF} = k_{-1}, \qquad k_{ex} = k_{FB} + k_{BF}, \tag{2.46}$$

where [H] is the concentration of the free host.

The association equilibrium constant is given according to

$$K = \frac{[\text{HG}]}{[\text{H}][\text{G}]} = \frac{k_1}{k_{-1}} = \frac{k_{FB}}{k_{BF}[H]} \tag{2.47}$$

(square brackets denote molar concentration).

The free molecules of host and guest may possess chemical shift different than the host-guest complex. The slow exchange regime is defined by a condition $k_{ex} \ll \Delta\omega$, where $\Delta\omega$ is the difference in resonating frequencies between free and complexed molecules. Under these conditions, we observe separate signals of each form.

NMR is a useful tool for studying the dynamics of chemical exchange process over a wide range of rates. Effective exchange rates k_{FB} and k_{BF} can be
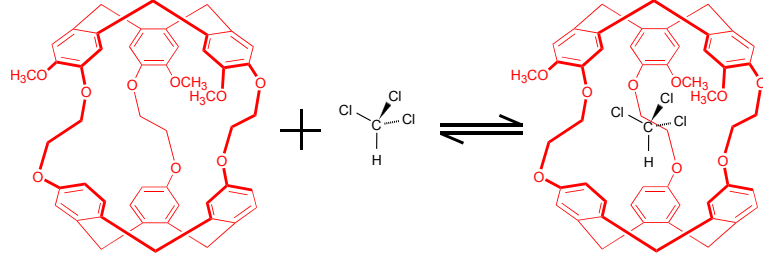
Figure 2.3: Illustration of host-guest complex formation.

determined by one- or two-dimensional magnetization transfer experiments, such as NOE experiments (see Section 3.5).

Even if the chemical exchange is slow on ^{1}H and ^{13}C chemical shift scale, it can still be comparable with the time scale of NMR relaxation and thus can affect significantly the apparent relaxation rates of species undergoing the exchange. In the presence of exchange, the modified Bloch equations 2.48 can be used to describe the time evolution of the longitudinal nuclear spin magnetizations towards the equilibrium

$$\frac{\mathrm{d}}{\mathrm{d}t}\begin{pmatrix} I_F \\ I_B \end{pmatrix} = \begin{pmatrix} -R_F - k_{FB} & k_{BF} \\ k_{FB} & -R_B - k_{BF} \end{pmatrix} \begin{pmatrix} I_F \\ I_B \end{pmatrix} + \\ + \begin{pmatrix} R_F & 0 \\ 0 & R_B \end{pmatrix} \begin{pmatrix} I_F^* \\ I_B^* \end{pmatrix}. \tag{2.48}$$

Equation 2.48 can be applied to describe the relaxation of the longitudinal magnetization of carbon-13 in chloroform molecules which belongs to the free (I_F) and bound (I_B) state. R_F and R_B are the longitudinal relaxation rates, related to the relaxation times as $R_F = 1/T_F$ and $R_B = 1/T_B$. I_F^* and I_B^* are NOE-enhanced carbon-13 intensities, at the steady-state in the presence of proton saturation, as they would be in case of no chemical exchange. These intensities are related to the NOE factors as follows: $I_F^* = \mathrm{NOE}_F I_F^0$ and $I_B^* = \mathrm{NOE}_B I_B^0$ where I_F^0 and I_B^0 are the equilibrium (unenhanced) carbon magnetizations for the free and bound site, respectively. When the exchange is present, the magnetizations at $t \to \infty$ (denoted as I_F^∞ and I_B^∞) can be obtained as a limit of the modified Bloch equations 2.48. The NOE factors for the two states (NOE_F, NOE_B) can be thus determined using the conventional dynamic NOE experiment according to:

$$\mathrm{NOE}_F = (1 + \eta_F) = \frac{k_{FB} I_F^\infty - k_{BF} I_B^\infty}{R_F I_F^0} + \frac{I_F^\infty}{I_F^0} \tag{2.49}$$

$$\mathrm{NOE}_B = (1 + \eta_B) = \frac{k_{BF} I_B^\infty - k_{FB} I_F^\infty}{R_B I_B^0} + \frac{I_B^\infty}{I_B^0}. \tag{2.50}$$

The last term in Equations 2.49 and 2.50 is the standard formula for determination of the steady-stare NOE values and the first term corresponds to the chemical exchange.

The overall strategy one can adopt for obtaining the relaxation rates in the free and bound states of chloroform is first to determine the exchange rates from selective 1D NOESY experiment (see Section 3.5), second to analyze ^{13}C inversion recovery or HSQC T_1 data according to the Equation 2.48 by employing previously measured exchange rates, and third to obtain the NOE parameters according to the dynamic NOE or HSQC NOE experiment (see Section 3.7) using Equations 2.49 and 2.50 and all parameters already determined.

2.6 Selected Aspects of Spin Relaxation

The principles of spin relaxation in NMR lie in the coupling of the spin system with the environment. Spontaneous and stimulated emission is not effective due to very small separations of energy levels. The mutual interactions between the spins and the interactions of spins with the surrounding, or the lattice, are responsible for fluctuating local magnetic field. These local fields can be decomposed by Fourier analysis into a superposition of harmonically varying magnetic fields with different frequencies. The component perpendicular to the static magnetic field $\boldsymbol{B}_0$ can induce transitions in the spin system. Such a transition is accompanied by the energy-conserving transition in the lattice. The lattice is assumed to be always in thermal equilibrium and has larger population in the lower energy state. Thus, transitions in the spin system from higher to lower state are more probable and the spin system is driven to equilibrium with the lattice.

There is also another phenomenon which does not include energy exchange. When the Larmor frequencies of the spin vary randomly, the phase coherence between spins is reduced over time. The fluctuations of the energy levels originate from the component of local magnetic field parallel to $\boldsymbol{B}_0$ and from the lifetime broadening due to the energy exchange described above. As a result, the relaxation of the spin coherences (associated with the transverse magnetization) differs principally from the relaxation of populations (connected to the longitudinal magnetization), and they are described by different characteristic time constants (T_2 and T_1, respectively). Extended theoretical explanation of the spin relaxation in liquids can be found for example in [11].

There is a range of physical interactions that can give rise to the fluctuations of local magnetic field capable of mediating spin relaxation. In the case of ^{13}C spins, it is molecular tumbling that modulates local magnetic field by means of chemical shielding anisotropy (CSA) interaction and direct dipolar coupling with directly attached protons. These are dominant mechanisms of carbon relaxation in diamagnetic systems.

2.6.1 Relaxation through Dipolar Interactions

The most efficient relaxation mechanism in the cryptophane-C and chloroform system is the dipole-dipole (DD) interaction between directly bonded ^{1}H and ^{13}C nuclei. Neglecting the non-dipolar mechanisms and the cross-correlated

relaxation between DD interactions, the longitudinal relaxation time T_1 and NOE factor $(1 + \eta)$ can be expressed in terms of *spectral densities* taken at linear combinations of ^{1}H and ^{13}C frequencies (Equations 2.51 and 2.52). The proportionality factor, the square of the dipole-dipole coupling constant, b_{CH}^2 (Equation 2.53), depends on the sixth power of the internuclear CH distance r_{CH} as well as several universal constants (permeability of vacuum μ_0, ^{13}C an ^{1}H magnetogyric ratios γ_C and γ_H and Planck constant $\hbar$). N_H denotes number of attached hydrogens

$$T_1^{-1} = \frac{1}{4}N_H(DCC)^2[J(\omega_H - \omega_C) + 3J(\omega_C) + 6J(\omega_H + \omega_C)] \quad (2.51)$$

$$\eta = \left(\frac{\gamma_H}{\gamma_C}\right)\frac{6J(\omega_H + \omega_C) - J(\omega_H - \omega_C)}{J(\omega_H - \omega_C) + 3J(\omega_C) + 6J(\omega_H + \omega_C)} \quad (2.52)$$

$$b_{CH}^2 = \left(\frac{\mu_0\gamma_H\gamma_C\hbar}{8\pi^2}\right)^2 r_{CH}^{-6}. \quad (2.53)$$

2.6.2 Spectral Density Function

The spectral density function $J(\omega)$ represents how much radiofrequency power is generated by fluctuating local magnetic fields at a particular frequency. It is a Fourier transform

$$J(\omega) = \int_{-\infty}^{\infty} C(\tau)e^{-i\omega\tau}\mathrm{d}\tau \quad (2.54)$$

of a *time correlation* function $C(\tau)$ which relates orientation of the molecule at two time moments separated by an interval τ (it is a sort of reorientational memory). Time correlation function is expected to be a decaying function for which $\lim_{\tau\to\infty} C(\tau) = 0$, the simplest choice might be exponentially decaying function

$$C(\tau) = C(0)e^{-|\tau|/\tau_c}, \quad (2.55)$$

where τ_c is called *correlation time*, which can be interpreted as a measure of time scale of oscillations of the random fluctuations. For time correlation function 2.55, spectral density is Lorentzian:

$$J(\omega) = C(0)\frac{2\tau_c}{1 + \omega^2\tau_c{}^2}. \quad (2.56)$$

2.6.3 Basic Equations of the Lipari-Szabo Approach

To express the frequency dependence of the spectral densities (and thus of the relaxation parameters), a certain model for molecular motion is needed to be adopted. Lipari and Szabo [12] proposed a simple model assuming isotropic reorientation of the molecule with the *global correlation time* τ_m, with addition of much faster restricted local motion of individual CH vectors, which

is assumed to be uncorrelated with the global motion. The local motion is described by two parameters: *generalized order parameter* S^2 (defining the degree of restriction) and the *local correlation* time τ_e. The Lipari-Szabo spectral density has the following form:

$$J_{LS}(\omega) = \frac{2}{5}\left[\frac{S^2\tau_m}{1+\omega^2\tau_m^2} + \frac{(1-S^2)\tau}{1+\omega^2\tau^2}\right], \qquad (2.57)$$

where $\tau^{-1} = \tau_m^{-1} + \tau_e^{-1}$. In the application of the Lipari-Szabo approach, a situation can arise in which the order parameter S^2 is quite high and the local correlation time τ_e is rather short, which allows neglecting the second term in Equation 2.57. This leads to truncated Lipari-Szabo spectral density [11]:

$$J_{LS,trunc}(\omega) = \frac{2}{5}\left[\frac{S^2\tau_m}{1+\omega^2\tau_m^2}\right]. \qquad (2.58)$$

If the order parameter in Equation 2.58 is set to $S^2 = 1$, spectral density for rigid body is obtained:

$$J_{RB}(\omega) = \frac{2}{5}\left[\frac{\tau_m}{1+\omega^2\tau_m^2}\right]. \qquad (2.59)$$

Part II

NMR Methodology

Chapter 3

Experimental Techniques

3.1 Inversion-Recovery

The spin-lattice relaxation time T_1 may be determined by using the *inversion-recovery* pulse sequence (see, for example, [11]), which is shown in Figure 3.1. The pulse sequence begins with a recycle delay t_{rd} that is sufficiently long to ensure that all magnetization returns to equilibrium. A π-pulse is applied which inverts the magnetization. The recovery delay vd follows to allow varying degree of T_1 relaxation. The final $\pi/2$-pulse then converts any z-magnetization into observable transverse magnetization. T_1 can be determined by repeating the experiment for different recovery delay values and fitting the resulting dependence of peak intensity on relaxation delays to exponentially recovering function.

For carbon-13 T_1 experiments, decoupling of protons throughout the measurement is usually applied to ensure that the relaxation is monoexponential.
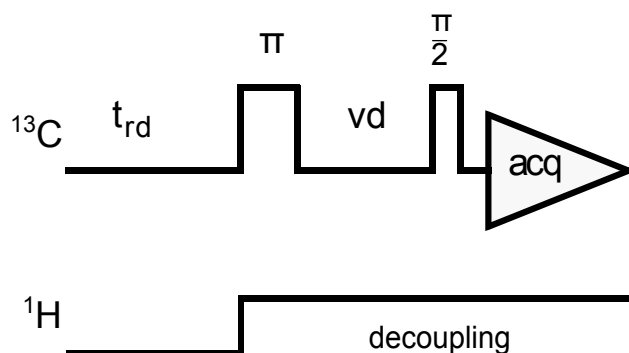
Figure 3.1: Inversion-recovery pulse sequence.

3.2 Steady-State NOE

Heteronuclear steady-state NOE factor can be obtain through two separate experiments (Figure 3.2) [11]. In the first experiment, protons are continuously
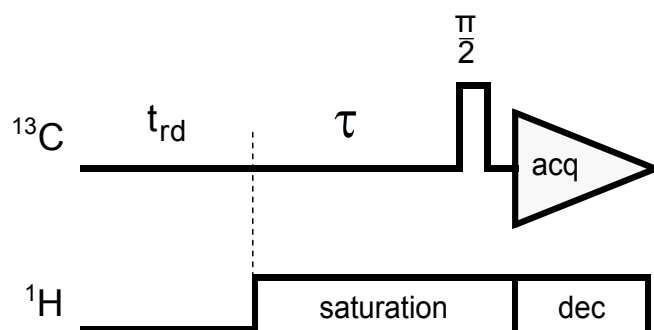
Figure 3.2: Steady-state NOE pulse sequence.

irradiated during a delay τ, which must be sufficiently long to ensure that NOE is built up to the maximum value. Then $\pi/2$-pulse to ^{13}C is applied and signal acquisition follows. The second experiment is performed without the irradiation. NOE factor is a ratio of signal intensities obtained by these two experiments.

3.3 Translational Diffusion

Using pulsed magnetic field gradient NMR experiments, translational diffusion can be measured. The simplest pulse sequence for measuring the translational diffusion is *modified spin echo* sequence, proposed by Stejskal and Tanner [13] (see Figure 3.3). First $\pi/2$-pulse creates transverse magnetization in the xy-plane. Then, magnetic field gradient of a duration δ, which causes spatial labeling of the spins, is applied. After the period τ, second π-pulse, which rotates the xy-plane through 180° around the y-axis, follows. Then, magnetic field gradient of a duration δ is applied again and spins are phased. Spin echo signal is observed after the period τ after the π-pulse. The application of the second gradient causes that only spins which did not change their position during the delay Δ between the gradient pulses are phased and therefore contribute to the echo.

Recently, more elaborate pulse sequences and experimental protocols have been developed in order to suppress effects of eddy currents, flow artifacts, as well as gradient imperfections. In our work, double stimulated echo sequence with bipolar gradients was used [14]. The pulse sequence is depicted in Figure 3.4. For some measurements, spin-lock was added before the acquisition to get rid of the minor phase distortions in the spectra [15], as depicted in Figure 3.5.

3.4 COSY

COrrelation **S**pectroscop**Y** (COSY) is a homonuclear 2D technique that is used to correlate the chemical shifts of ^1H nuclei which are J-coupled to one
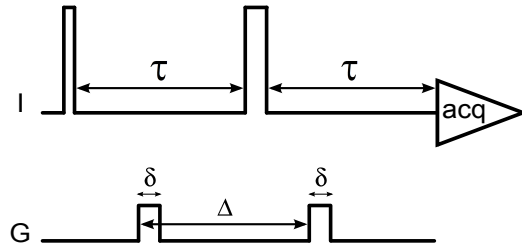
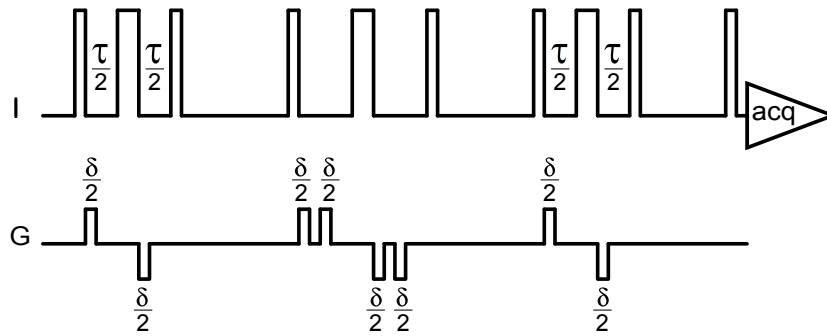Figure 3.3: The Stejskal-Tanner modified spin echo experiment for measuring translational diffusion.

Figure 3.4: Double stimulated echo sequence with bipolar gradients.
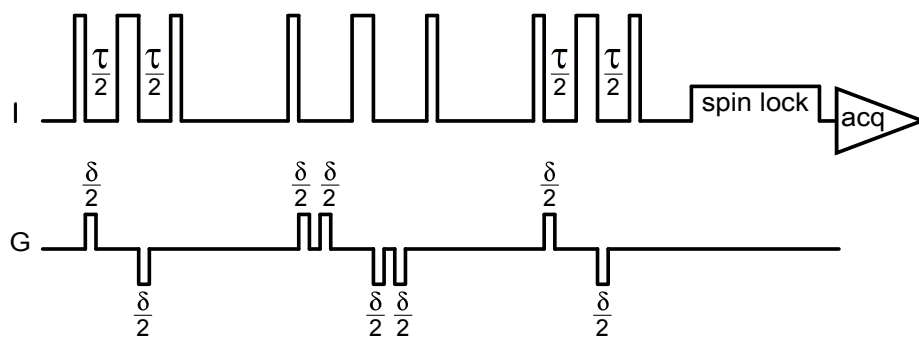

Figure 3.5: Double stimulated echo sequence with bipolar gradients and with spin-lock before acquisition.
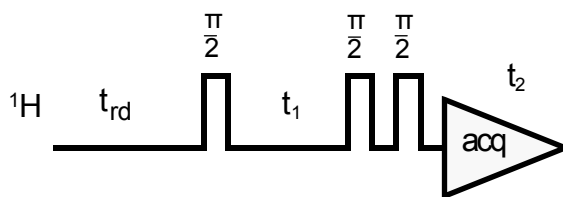
Figure 3.6: DQF-COSY pulse sequence.

another.

Special type of COSY experiment is Double Quantum Filtered COSY (DQF-COSY), which deals with a few drawbacks that appear in simple magnitude mode COSY. The first problem is the anti-phase structure of the crosspeak multiplet while diagonal peaks have in-phase structure. The second problem is the double dispersion lineshape of the diagonal peaks. In contrast, in the DQF-COSY all of the multiplets are in anti-phase and all the peaks are in absorption mode. This results in spectra with a better balance of intensity between the crosspeaks and diagonal peaks.

Pulse sequence for measuring DQF-COSY is a three-pulse sequence (shown in Figure 3.6) and can be explained as follows [16]: the first pulse, the preparation pulse, creates transverse magnetization components for all allowed transitions. This is followed by the evolution period t_1 during which the various magnetization components are labeled with their characteristic precession frequencies (including chemical shift and homonuclear J-coupling). The mixing pulse then transfers magnetization components among all those transitions that belong to the same coupled spin system. The third pulse follows immediately after the second pulse and ensures that the signals observed during t_2 all derive from double-quantum coherence present between the second and third $\pi/2$-pulses. This is achieved by a coherence selection method such as phase cycling or pulse field gradients. Then, only spins which exhibit multiple-quantum coherence after the second pulse are detected during t_2. This means that only spins that are J-coupled to at least one other spins are detected. The COSY spectrum is produced by a 2D Fourier transform with respect to t_1 and t_2, and its crosspeaks indicate which ^{1}H nuclei are J-coupled.

3.5 NOESY

Nuclear **O**verhauser **E**ffect **S**pectroscop**Y** is a 1D or 2D spectroscopy method whose aim is to identify spins undergoing cross-relaxation and to measure cross-relaxation rates [11]. Most commonly, NOESY is used as a homonuclear ^{1}H technique. In NOESY, direct dipole-dipole couplings provides the primary means of cross-relaxation, and so spins undergoing cross-relaxation are those which are close to one another in space. Thus, the crosspeaks of a NOESY spectrum indicate which ^{1}H nuclei are close to each other in space.

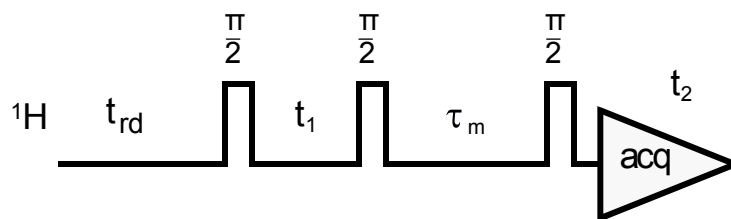The basic NOESY pulse sequence (see Figure 3.7) consists of three $\pi/2$-pulses.

31

Figure 3.7: NOESY pulse sequence.

The first pulse creates transverse magnetization, which precesses during the evolution period t_1 (increased during the course of the 2D experiment). The second pulse creates longitudinal magnetization equal to the transverse magnetization component orthogonal to the pulse direction. The aim is to produce initial situation for the mixing period τ_m (during which cross-relaxation occurs) where the longitudinal polarization of each spin is labeled by its resonance frequency. The longitudinal magnetization is allowed to relax during the mixing time τ_m. For basic NOESY experiment, τ_m is kept constant throughout the 2D experiment. The third pulse creates transverse magnetization from the remaining longitudinal magnetization. Acquisition begins immediately following the third pulse, and the transverse magnetization is observed as a function of t_2. For the coherence pathway selection, appropriate phase cycling is needed. The NOESY spectrum is generated by a Fourier transform with respect to t_1 and t_2.

Chemical exchange, if present, can also lead to the magnetization transfer and thus to the appearance of the crosspeaks in NOESY spectrum if the exchange rate is not slow compared to the mixing time. That allows to use NOESY for determining exchange rates. In this case, the selective 1D NOESY pulse sequence with pulsed field gradients [17] can be used. The sequence is shown in Figure 3.8 and can be described as follows: The first block of the sequence is based on so-called excitation sculpting procedure, during which one of the sites is selectively inverted. Second block contains variable mixing time, during which the magnetization transfer caused by exchange occurs. Then the signal is detected from the second site by the last 90-degree pulse. During the experiment, pulsed field gradients (G) are applied. As a result, one obtains the exchange-mediated buildup of the other ^{1}H signal as a function of mixing time interval.

Assuming that intervals are sufficiently short for observing the process in the initial rate regime, the intensity from the signals of the second site increases linearly with the mixing time. Effective reaction rates are given by a slope of the buildup curve.

3.6 ROESY

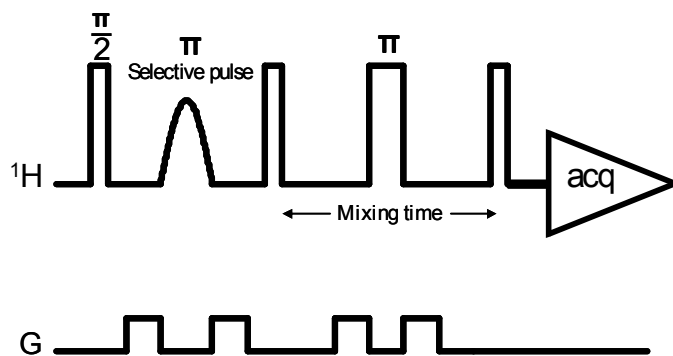**R**otating-frame **O**verhauser **E**ffect **S**pectroscop**Y** is an experiment in which

Figure 3.8: Pulse sequence for selective 1D NOESY experiment for determination effective chemical exchange rates.
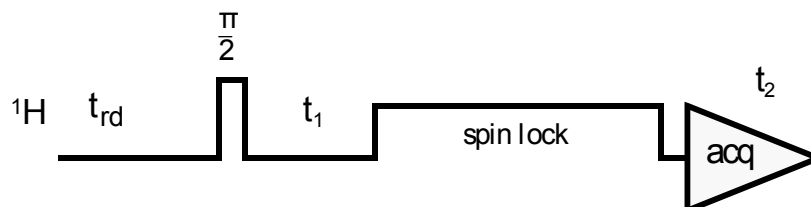

Figure 3.9: ROESY pulse sequence

homonuclear NOE effects are measured under spin-lock conditions [11]. This experiment deals with several problems that can occur by measuring NOESY.

It is especially suited for molecules with motional correlation time τ_c such that $\omega\tau \approx 1$, where ω is the angular frequency, $\omega = \gamma B$. In such cases the laboratory-frame NOE is nearly zero, but the rotating-frame NOE (or ROE) is always positive and increasing monotonically for increasing values of τ_c.

ROESY is also useful when chemical exchange is present and exchange crosspeaks would appear in NOESY spectrum.

ROESY pulse sequence is shown in Figure 3.9. In ROESY, the mixing time is the spin-lock period. During this time spin exchange occurs among spin-locked magnetization components of different nuclei (unlike in NOESY, where the spin exchange occurs while magnetization is aligned along the z-axis).

3.7 HSQC

Heteronuclear **S**ingle-**Q**uantum **C**orrelation **S**pectroscopy is a 2D experiment which can be used for measuring relaxation parameters, using indirect detection [16]. A general form of the pulse sequence is presented in Figure 3.10 A. The pulse sequence contains INEPT (Insensitive Nuclei Enhancement by Polarization Transfer) block, during which the I spin polarization is transferred to the S spin. The S spin magnetization evolves for t_1, during which it acquires

a frequency label according to the offset of S. Finally, this magnetization is transferred by reverse INEPT back to I, where it is observed. The resulting spectrum thus has peaks centered at the offset of the spin S in ω_1 dimension, and at the offset of the spin I in the ω_2 dimension.

HSQC-type of experiment can be used both for measuring longitudinal relaxation times T_1 and dynamic heteronuclear NOE [11].

Pulse sequence used in the first case is shown in Figure 3.10 B. At the beginning, refocused INEPT is used to create enhanced transverse magnetization on the less sensitive nuclei. Following $\pi/2$-pulse on S spin creates non-equilibrium longitudinal magnetization that is allowed to relax during the relaxation period τ. Afterwards, reverse INEPT is applied to transfer the magnetization back to I spin, where it is detected. Two-dimensional, inverse-detected series of spectra for different relaxation delays are obtained. The crosspeak volume integrals are determined and fitted to an exponentially decaying function.

Pulse sequence used in case of measuring dynamic NOE can be seen in Figure 3.10 C. The overall scheme begins with a delay, during which proton saturation is or is not present. Then, transverse magnetization on the S spin is created by $\pi/2$-pulse. Magnetization evolves during the t_1 period and then is transferred by reverse INEPT to the I spin, where it is detected. Two separate measurements are carried out, with and without proton irradiation. The ratio of intensities by these two experiments provides information about NOE enhancement.

3.8 HMBC

Heteronuclear **M**ultiple **B**ond **C**orrelation spectroscopy is a 2D inverse detected experiment suitable for determining long-range ^{1}H - ^{13}C connectivity. This is useful in determining the structure and ^{1}H and ^{13}C assignment of molecules.

The HMBC pulse sequence (see Figure 3.11) may be described simply as follows [16]: During period τ, magnetization is excited and allowed to become anti-phase. It is then transferred to multiple-quantum coherence by the first S-spin pulse. After evolution for t_1, the coherence is transferred back into anti-phase magnetization on the spin I by the second S-spin pulse. The signals are observed immediately after the coherence transfer step. The optimum value for τ is $1/(2J_{IS})$. Pulsed field cleaning gradients (G) are applied during the experiment. The 2D spectrum is generated by a Fourier transform with respect to t_1 and t_2.
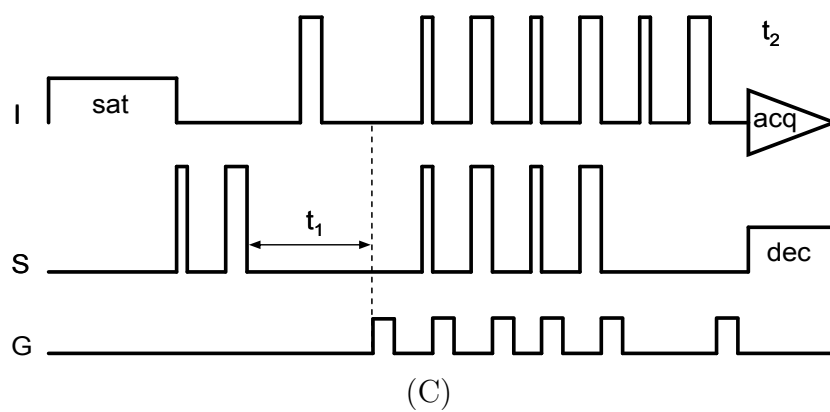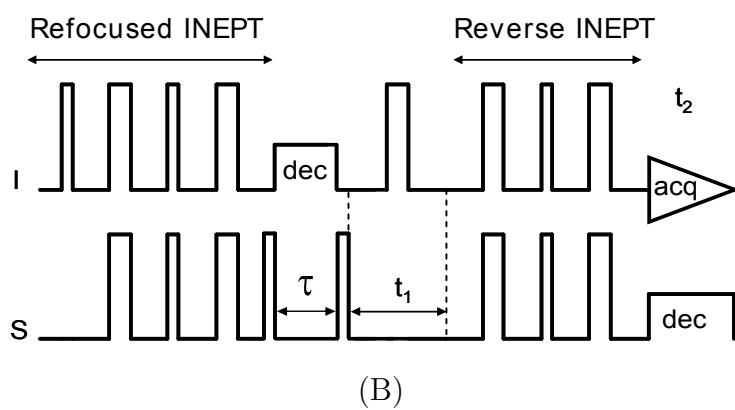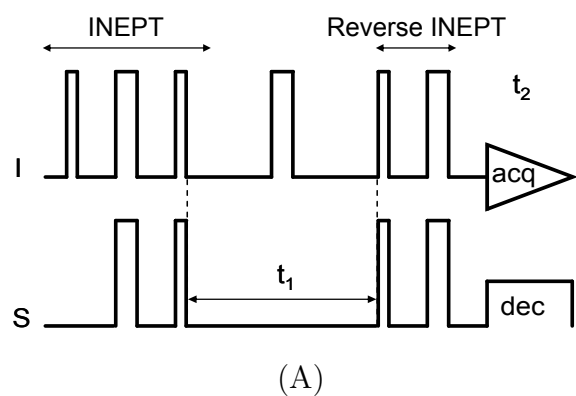
Figure 3.10: Different modifications of HSQC pulse sequence, (A) Basic HSQC, (B) HSQC for T_1 measurements, (C) HSQC for NOE measurements.
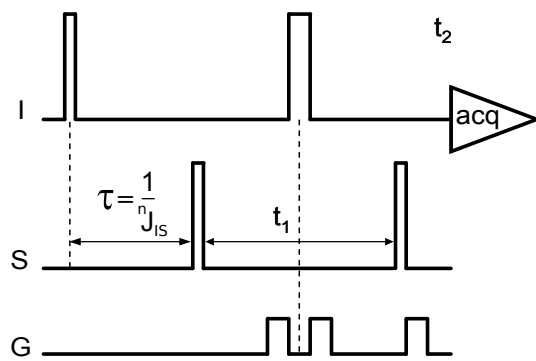
Figure 3.11: HMBC pulse sequence

Part III

NMR Investigation of Host-Guest Complexes between Cryptophane-C and Chloroform

Chapter 4

Cryptophanes

Since the origin of the concept of host-guest chemistry, a wide variety of synthetic organic compounds, which can form self-organized systems, have been prepared and studied. Those complexes have possible applications in molecular recognition, drug delivery, separation and storage, catalysis, and many others [1].

Special type of molecules which have guest binding ability are *cryptophanes* [18]. Chemical structure of cryptophanes is based on two (possibly modified) cyclotriveratrylenes (CTVs) (see Figure 4.1) adjacent to each other and linked covalently with $-(CH_2)_n-$ and possibly other bridges. Consistent with their encapsulating nature, cryptophanes possess remarkable binding ability for small, tetrahedral molecules such as methane and its halogenated derivates.

Many types of cryptophanes with different substituent groups have been synthesized, this work focuses especially on cryptophane-C molecule (shown in Figure 4.2) and its interaction with ^{13}C labeled chloroform dissolved in 1,1,2,2-tetrachloroethane.
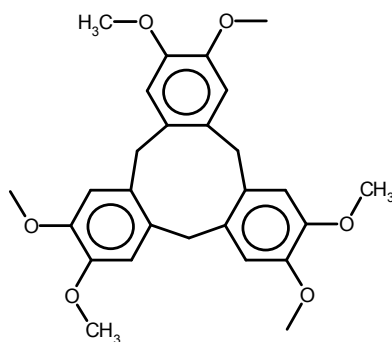

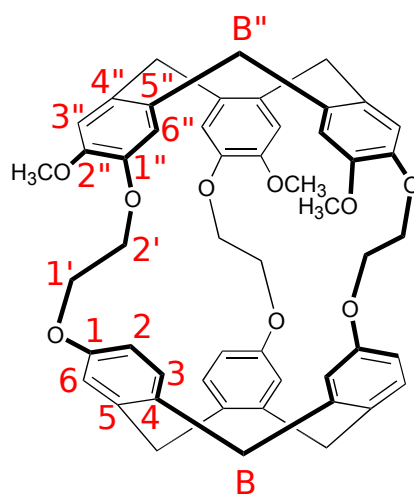Figure 4.1: Cyclotriveratrylene unit (CTV).

Figure 4.2: Cryptophane-C. Carbon atom numbering used for the NMR spectra assignment is shown for non-methoxylated aromatic rings (1 - 6), methoxylated aromatic rings (1" - 6"), CH_2 linkages (1', 2') and methylene bridges (B, B").

Chapter 5

Experimental Section

5.1 Sample

Sample studied in this work consists of cryptophane-C, concentration of 10.7 mM (prepared in the organic chemistry laboratory in Lyon [19]), ^{13}C-labeled chloroform $CHCl_3$, concentration of 60.2 mM (Cambridge Isotope Laboratories), dissolved in deuterated 1,1,2,2-tetrachloroethane (Cambridge Isotope Laboratories). The sample was degassed by the freeze-pump-thaw procedure several times and flame-sealed in a 5 mm NMR tube.

5.2 Experimental Settings

All NMR experiment were carried out with Bruker Avance spectrometers with resonance frequencies for proton nuclei of 400 MHz (magnetic field of 9.4 T) and 600 MHz (magnetic field of 14.1 T). Temperature of measurements was chosen to be sufficiently low to ensure slow chemical exchange, but higher than the temperature at which crystallites start to occur in the sample. The temperature calibration was done prior to each experiment using a standard pure methanol calibration sample.

For measurements on protons, BBI probe was used and for measurements on carbon-13, BBO probe was used.

The chemical exchange reaction rates were measured with 'SELNOGP' pulse sequence with one selective 180-degree pulse in the excitation part. The shape of the selective excitation pulse was Gaussian cascade 'Gauss5' covering the first peak of the chloroform signal. The length of the shaped pulse was $15-20$ ms and the power was between 40 and 60 dB (parameter 'sp2'), calibrated by using 'SELGPSE' sequence.

For inversion-recovery and dynamic NOE measurements, 'WALTZ-16' proton decoupling scheme was used, for HSQC T_1 measurements, 'DIPSY2' proton decoupling and 'GARP' carbon decoupling scheme was applied.

Chapter 6

Results and Discussion

6.1 Signal Assignment

^{1}H and ^{13}C spectra of cryptophane-C with chloroform are rather complicated and contain groups of signals from cryptophane-C, chloroform and the solvent. For signal assignment in the carbon and proton spectra, additional 2D experiments such as DQF-COSY, HSQC and HMBC had to be applied.

DQF-COSY can be found as a useful experiment, since it allows us to determine signals of mutually J-coupled protons. Figure 6.1 shows the DQF-COSY spectrum of cryptophane-C. Three areas of mutually coupled cryptophane-C protons can be recognized in the spectrum: aromatic protons (denoted as $1-6$ in non-methoxylated rings and $1" - 6"$ in methoxylated rings), protons in $-(CH_2)_2-$ linkages between the CTV units (denoted as 1' and 2') and protons in methylene bridges within the CTV unit (denoted as B in non-methoxylated rings and B" in the methoxylated rings).

HSQC experiment allows us to determine carbons and protons which are directly bonded to each other and thus is helpful for assigning both proton and carbon spectra. HSQC spectrum of cryptophane-C and chloroform is presented in Figure 6.2. It is again possible to recognize areas for aromatic signals (Figure 6.2 A) and signals from $-(CH_2)_2-$ linkages between the CTV units and methylene bridges within the CTV units (Figure 6.2 B) .

However, HSQC experiment does not provide for assignment of carbons without directly bonded protons. For this purpose, HMBC spectrum can be useful. HMBC spectrum shows long-range ^{1}H $-^{13}$C couplings, mainly three-bond J-coupling. For cryptophane-C and chloroform, HMBC spectrum at 250 K and 400 MHz is shown in Figure 6.3. Marked crosspeaks were important for assigning ^{13}C spectrum (Figure 6.4 B).

The final assignment for the ^{1}H and ^{13}C signals is shown in Figure 6.4.

Chloroform signals in ^{1}H spectrum appear as a dublet plus singlet corresponding to the ^{12}C species and overlaps slightly with cryptophane-C aromatic signal. Due to the mutual slow exchange on ^{1}H chemical shift scale, separate signals of bound and free chloroform guest molecules can be observed. The ^{1}H resonance of the bound molecule is at 2.55 ppm, shifted upfield by 4.74 ppm compared to the free molecule. This is caused by the shielding effect of the
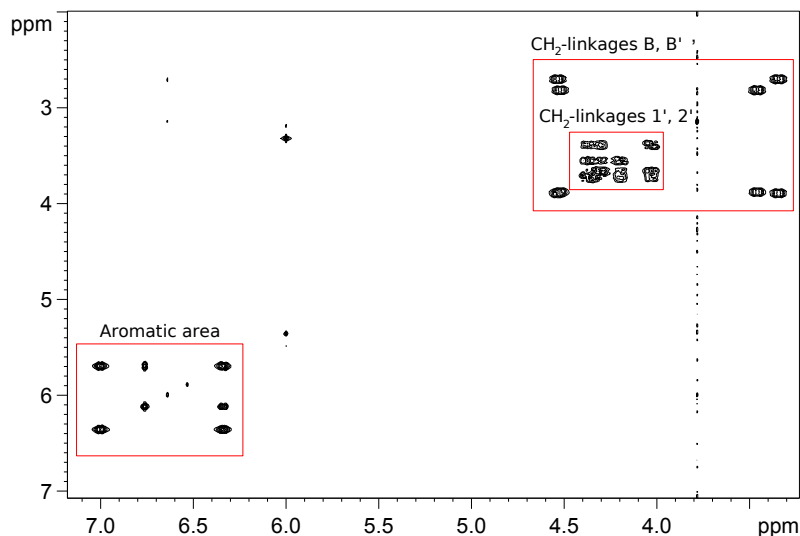
Figure 6.1: DQF-COSY spectrum of cryptophane-C at 268 K, 400 MHz. Three areas of mutually J-coupled protons can be recognized.

cyclotriveratrylene units.

However, it is not possible to distinguish between signals for bound and free cryptophane in ^{1}H spectrum, nor can they be reliably recognized in ^{13}C spectrum.

6.2 Orientation of the Guest in the Host Cavity

Previous studies [20] showed that chloroform (unlike dichloromethane) behaves as an integral part of the host molecule (cryptophane-E) after inclusion in its cavity and no fast large scale motion was observed. This behaviour of chloroform raised a question about the orientation of chloroform inside the cryptophane. The idea was to study cryptophane molecule which is asymmetrical and thus enables to distinguish between the possible guest orientations.

Cryptophane-C, thanks to its asymmetry, is sufficient for the investigation of preferred orientation of the chloroform molecule inside the host cavity. One of the two CTV units of cryptophane-C is modified so that it does not contain methoxy groups. This asymmetry influences positions of both ^{1}H and ^{13}C resonances in the spectra of cryptophane-C. Signals from the methoxylated and non-methoxylated aromatic rings can be recognized at different positions in the spectra (as already mentioned in Section 6.1). This applies also for ROESY spectrum (shown in Figure 6.5), where crosspeaks between bound chloroform and aromatic protons from the two different parts of cryptophane-C molecule can be distinguished.
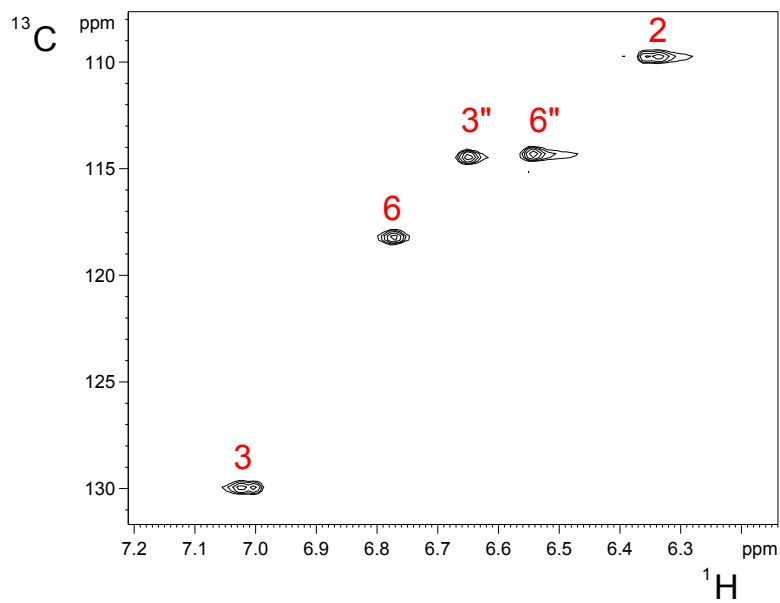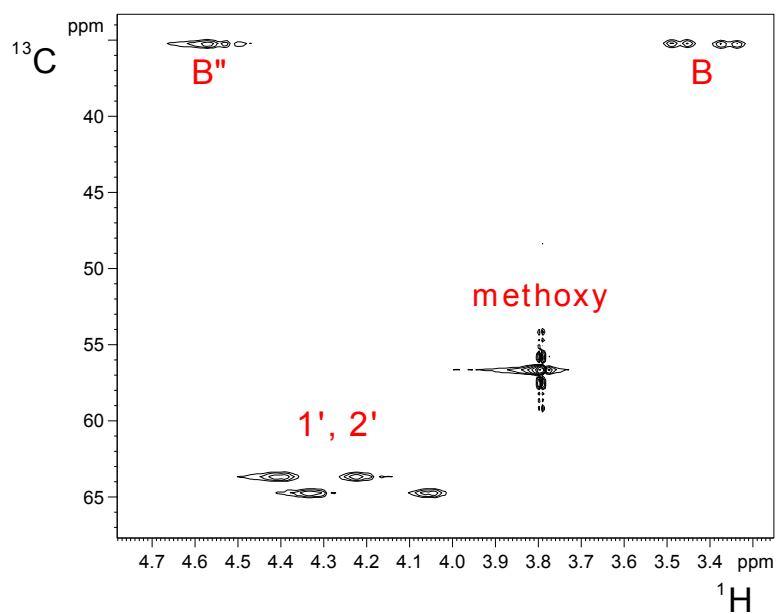
Figure 6.2: (A) Aromatic part and (B) CH$_2$ linkage part of the HSQC spectrum of cryptophane-C and chloroform at 268 K, 400 MHz.
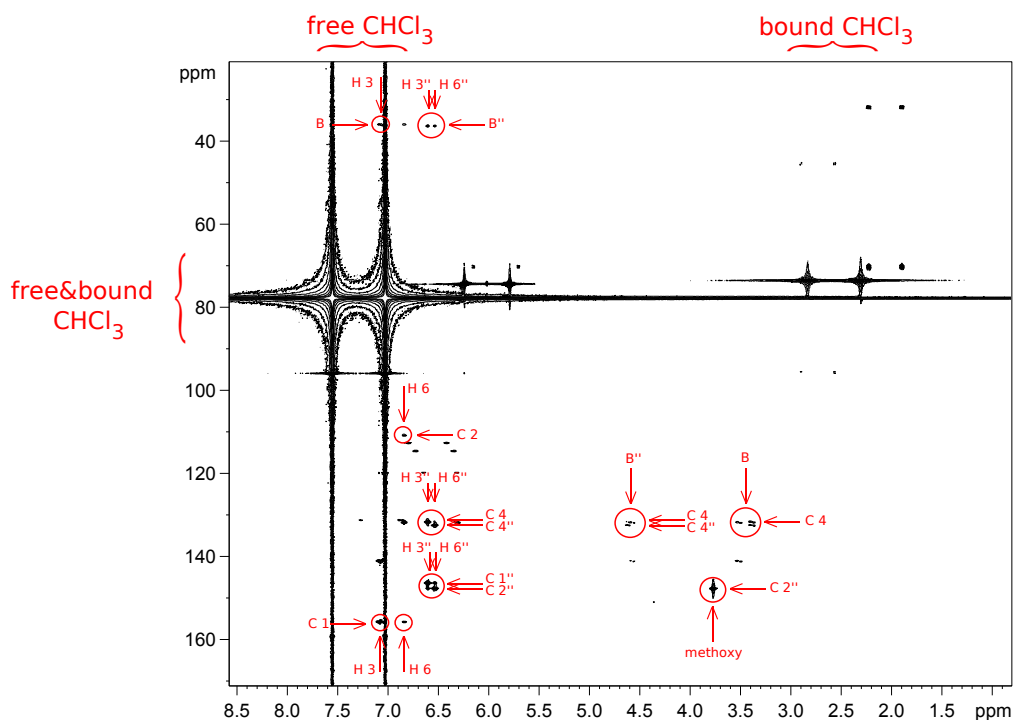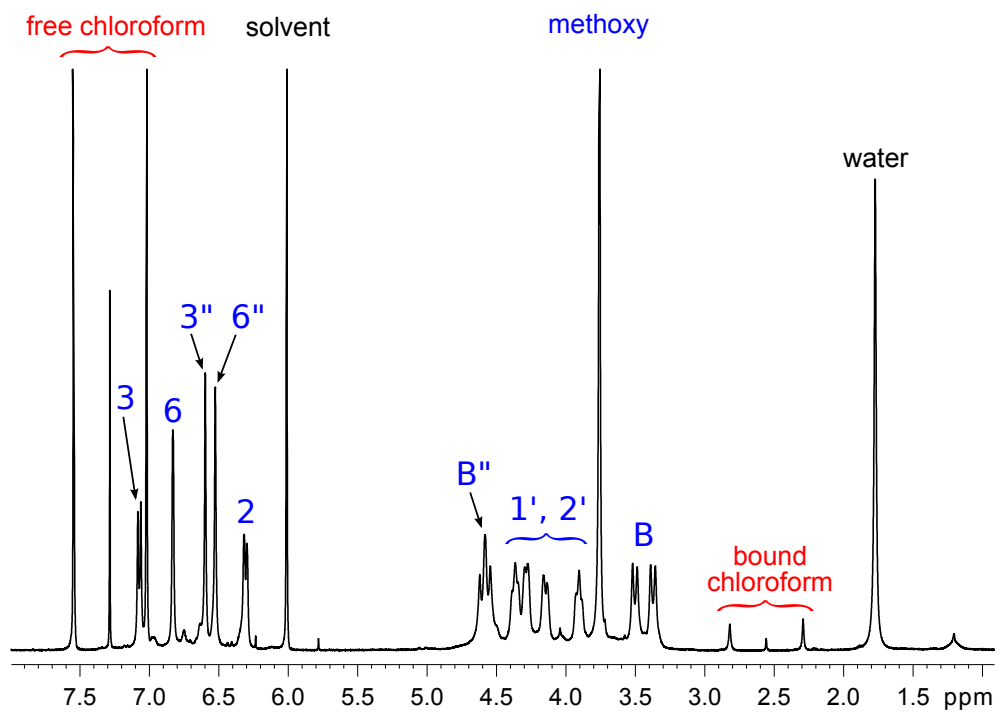
Figure 6.3: HMBC spectrum of cryptophane-C and chloroform at 250 K, 400 MHz. Peaks important for assignment are marked.

Since ROESY spectrum shows crosspeaks between protons which are close in space, it is possible to estimate which aromatic protons are close to the chloroform proton. The more intensive crosspeak, the more probable is the corresponding orientation.

ROESY spectra were recorded with mixing time of 200 ms at 246 and 250 K at 600 MHz spectrometer. Both spectra have very similar patterns, intensities of the crosspeaks between chloroform proton and host aromatic protons are presented in Table 6.1. Despite of our expectations, crosspeaks between the guest signals and aromatic host signals had very low intensity and no other crosspeaks between host and guest signals were observed. The most intensive crosspeaks were between chloroform proton and proton attached to carbon 6 at the host molecule (in non-methoxylated benzene rings). However, the accuracy of the integrals of such a low signals is disputable. It may be probable that the preferred orientation of guest molecule is with hydrogen pointing to the non-methoxylated part and chlorines pointing to the methoxylated part of cryptophane-C molecule. To make this result trustful, it would be necessary to support it by other methods, for example by theoretical calculations.

6.3   Kinetics of the Complex Formation

Important step in the analysis of the complex formation is to determine the effective chemical exchange rates k_{FB} and k_{BF} of the guest entering and leaving
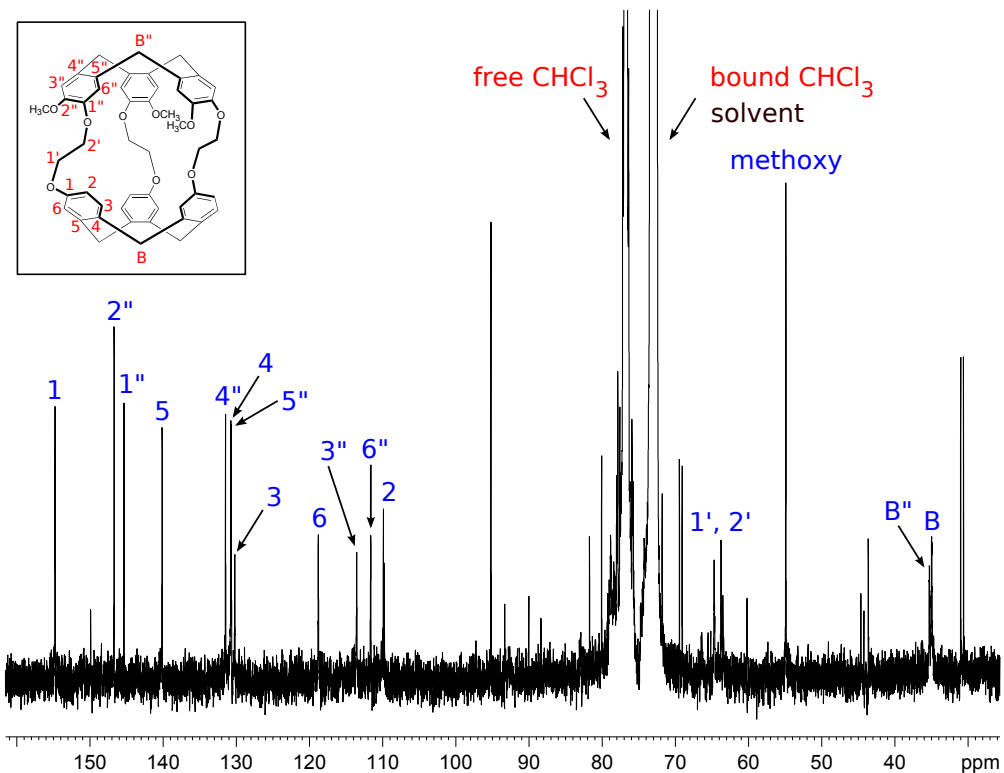
Figure 6.4: Assigned spectra of cryptophane-C and chloroformat 400 MHz, (A) ^{1}H spectrum, (B) ^{13}C spectrum.

			bound chloroform [ppm]		
			2.719	2.545	2.368
aromatic	2	6.294	0.47	0.15	0.48
protons	3", 6"	6.539	0.75	0.19	0.77
[ppm]	6	6.830	0.95	0.24	1.00

<div align="center">(A)</div>

			bound chloroform [ppm]		
			2.727	2.550	2.373
aromatic	2	6.308	0.51	0.12	0.52
protons	3", 6"	6.489	0.75	0.20	0.79
[ppm]	6	6.830	0.97	0.25	1.00

<div align="center">(B)</div>

Table 6.1: Relative integrals of ROESY crosspeaks at (A) 246 K and (B) 250 K, 600 MHz with ROESY mixing time 200 ms.
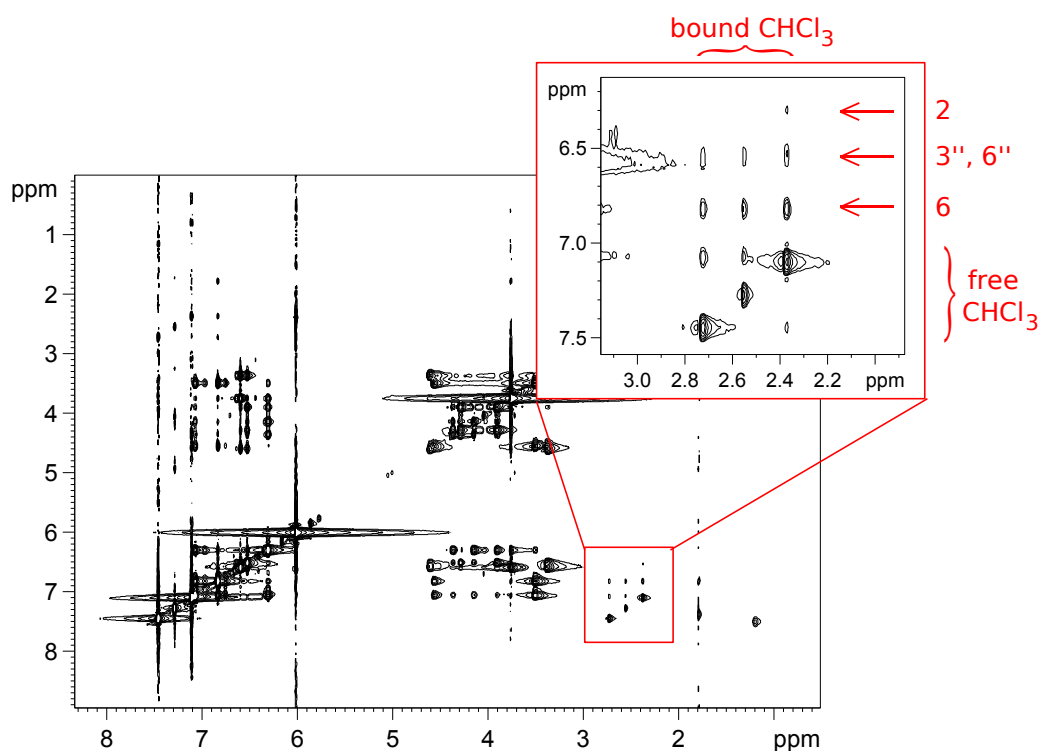

Figure 6.5: Detail of crosspeaks between bound chloroform and aromatic protons in methoxylated and non-methoxylated rings in ROESY spectrum of cryptophane-C and chloroform at 250 K, 600 MHz with mixing time 200 ms.

the host cavity. Slow chemical exchange between both sites together with the shielding effect of the CVT units ensures well separated signals from both sites. That allows us to use selective 1D NOESY experiment (described in Section 3.5).

Mixing times in the experiments were arranged in equal steps from a very short mixing time to the value at which approximately $10-30\%$ of the magnetization was transferred. By measuring the dependence of transferred magnetization on the mixing time, a buildup of the signal at the second site is obtained. Magnetization transfer from free to the bound guest (bound buildup) allows determination of the free-to-bound effective reaction rate k_{FB}, and vice versa.

The intensity of the excited signal was extrapolated to the zero mixing time and intensities of the buildup were normalized according to this value. Buildup intensities were fitted to a second order polynomial function and the effective exchange rates were determined as the coefficient at the linear term. This procedure is called initial rate approximation and can be used if mixing times are sufficiently short in chosen range, which is fulfilled in our case.

Typical build-up and decay curves of the chloroform signal intensities are shown in Figure 6.6. A better fit is always obtained for free-to-bound magnetization transfer, which is a result of the lower intensity (and thus the signal-to-noise ratio) for the resonance of the bound guest. The reason for this is that the concentration of the bound guest is limited by the concentration of the cryptophane-C and is also attenuated by the fairly low association constant of the complex. Estimated relative error for the free-to-bound rate k_{FB} is 10% and for the bound-to-free rate k_{BF} is 15%.

The effective exchange rates k_{FB} and k_{BF}, obtained at different temperatures, are presented in Table 6.2. Constants k_1 and k_{-1} were calculated according to the Equations 2.46, the concentration of the free host [H] was obtained by using integrals of the proton signals of the bound and the free site and known concentration of the cryptophane and chloroform within the sample. Relative error of [H] was estimated as 11%.

The temperature dependence of the exchange rates is illustrated in the Arrhenius plot in Figure 6.7. Activation energies E_A are extracted by fitting the data to the Arrhenius equation

$$k = A \exp\left(-\frac{E_A}{RT}\right), \tag{6.1}$$

where k is either k_1 for the direct reaction or k_{-1} for the reverse reaction. Obtained activation energies are presented in Table 6.3.

The association equilibrium constant was calculated both according to the Equation 2.47 and to the integrals of free and bound signals in ^{1}H spectra. Results together with estimated relative errors are presented in Table 6.4.

The association constant appears to be fairly low, which means that the equilibrium is shifted towards free host and guest rather than towards the complex. This is also apparent if we consider the reaction rates - the free-to-bound rates are much lower than the bound-to-free reaction rates. Also the concentration of the free host implies that there are approximately four times
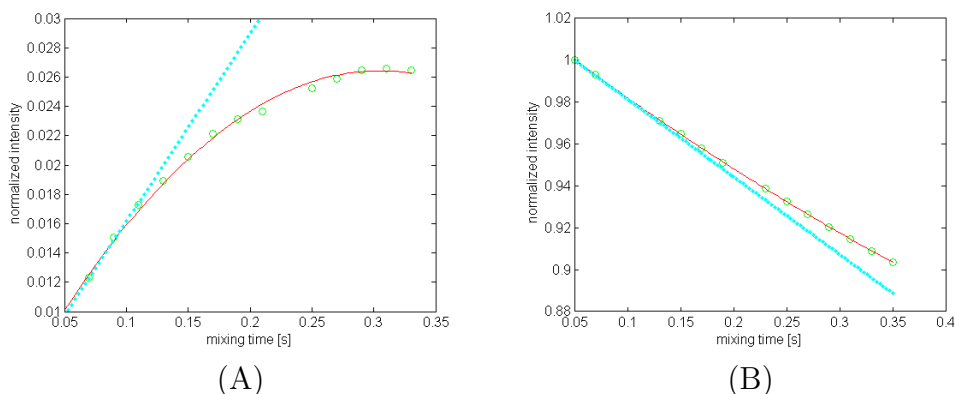
Figure 6.6: Free-to-bound magnetization transfer, (A) shows the building-up magnetization of the bound site, (B) shows the decaying magnetization of the free site.

T [K]	k_{FB} [s^{-1}]	k_{BF} [s^{-1}]	[H] [mM]	k_1 [s^{-1}.M^{-1}]	k_{-1} [s^{-1}]
246	0.048	1.1	7.8	6.1	1.1
250	0.076	2.3	7.8	9.7	2.3
254	0.150	3.9	8.0	18.8	3.9
258	0.177	5.7	7.9	22.4	5.7
rel. error	10%	15%	11%	15%	15%

Table 6.2: Exchange rates for both sites.

more free host molecules than bound in the complex. This is rather unexpected result considering that in the previous studies [21, 22], similar concentrations of host and guest were used and, unlike in our study, equilibrium was shifted significantly towards the complex and the free host concentration was lower than in our case. This may indicate either that cryptophane-C is not very well accepting chloroform as a guest, or presence of impurities within the sample, which may compete with chloroform in complex formation.

Poor accuracy of association constant determination is due to accumulation of rather high uncertainties of reaction rates k_{FB} and k_{BF} and free host concentration [H].

The equilibrium constant hardly shows temperature dependence in measured temperature range, thus it was not possible to investigate the thermodynamic parameters such as complexation enthalpy and entropy.

	E_A [kJ.mol^{-1}]
free-to-bound	52
bound-to-free	64

Table 6.3: Activation energies.

T [K]	K [M^{-1}] from rates	K [M^{-1}] from integrals
246	5.6	6.4
250	4.2	6.5
254	4.9	6.0
258	3.9	6.1
rel. error	21%	13%

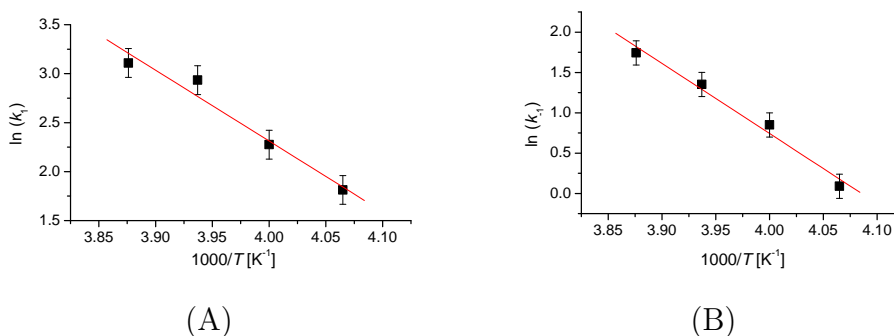Table 6.4: Equilibrium constants.

(A)

(B)

Figure 6.7: Arrhenius plot (A) for the free-to-bound reaction and (B) for the bound-to-free reaction.

6.4 Relaxation Parameters

Carbon-13 longitudinal relaxation times T_1 and heteronuclear NOE were measured for both host (cryptophane-C) and guest (chloroform) molecule. Measurements were carried out at the temperature of 250 K and at the magnetic field of 9.4 T (400 MHz) and 14.1 T (600 MHz). Since the relaxation behaviour and carbon-13 signal intensity of the host and the guest is not the same, different experimental techniques needed to be applied.

As for the host relaxation, HSQC T_1 experiments were used to obtain longitudinal relaxation times and HSQC NOE experiments were applied to obtain NOE factors (described in Section 3.7). Data were obtained by taking the volume integrals of the aromatic area in the HSQC spectrum of cryptophane-C (see Figure 6.2 A) and fitting them to exponentially decaying function.

Considering that there is no evident difference in chemical shifts of free and bound host neither in ^{13}C spectrum nor in ^{1}H spectrum, measured values have contribution of both species (weighted according to the their relative abundance). Due to the calculation of free host concentration (Table 6.2), the population of the free host is approximately four times higher then of the bound species. However, we expect that the presence of the guest is not likely to have a major effect on the host mobility.

Obtained values of ^{13}C longitudinal relaxation times T_1 and NOE factors for aromatic carbons are presented in Table 6.5. Measured relaxation times

Carbon	3	6	3", 6"	2
T_1 [s]	0.20	0.20	0.14	0.14
NOE	1.30	1.27	1.26	1.27

Table 6.5: Longitudinal relaxation times and NOE factors of Cryptophane-C aromatic carbons at 250 K, 400 MHz.

are rather short and NOE values are significantly less then 3, which provide an indication that their relaxation is outside of the extreme narrowing regime. However, to confirm this assumption, relaxation parameters measured at at least one more field would be useful. One can also discuss the chemical shielding anisotropy (CSA) contribution to the nuclear relaxation of cryptophane-C aromatic carbons. According to the previous studies [20, 21], CSA can play important role in case of aromatic carbons relaxation in other cryptophanes. To shed light upon this problem, relaxation times for other carbons in the molecule would have needed to be measured in order to compare their relaxation with already measured carbons.

Concerning the guest relaxation, the ^{13}C-labeled chloroform allowed us to measure relaxation properties with direct carbon detection. Longitudinal relaxation times for the free and bound guest were measured using inversion-recovery (see Section 3.1) and NOE factors were obtained by steady-state NOE experiments (see Section 3.2) at 600 MHz. Only for NOE measurement at 400 MHz, we used HSQC NOE experiments (see Section 3.7), because the bound chloroform signal has low intensity and is very close to the solvent signal.

Because of the chemical exchange between the two sites taking place on the similar timescale as the longitudinal relaxation, it was necessary to use a more elaborate approach (as described in Section 2.5) to extract the relaxation times of the guest from the signal intensities. The first step - the assessment of the exchange rates - was already presented in Section 6.3. In the second step we considered these rates as fixed and plugged them to the Equation 2.48 in order to fit the time course of signal intensities corresponding to free and bound state of chloroform, and thus determine the relaxation rates R_F and R_B. In the last step, all of these values were then employed in Equations 2.49 and 2.50 and the NOE_F and NOE_B were calculated.

Disadvantage of this approach is that the experimental error of each step is directly introduced into the next one. This is the reason of rather high uncertainty of calculated NOE values, which accumulates all the errors of parameters involved in Equations 2.49 and 2.50. Error estimation was based on Monte Carlo (MC) simulation of each computation step.

Obtained values for longitudinal relaxation times and NOE factors for bound and free chloroform are presented in Table 6.6 together with the estimated errors. In MC simulations, a variation of the measured intensities on 2% level for the free guest and 5% level for the bound guest (which signal has much lower intensity) was used. Parameter errors calculated at one step of the analysis were used in the simulations of the following steps. Relaxation

	9.4 T (400 MHz)		14.1 T (600 MHz)	
	T_1 [s]	NOE	T_1 [s]	NOE
Free CHCl$_3$	4.40 (4.0%)	2.70 (3.1%)	4.59 (5.2%)	2.73 (3.1%)
Bound CHCl$_3$	0.16 (2.1%)	1.2 (18%)	0.33 (2.5%)	1.6 (10%)

Table 6.6: Longitudinal relaxation times and NOE factors of bound and free chloroform at 250 K. In parentheses are relative errors from the Monte Carlo analysis.

rates R_F and R_B differ enough to get reliable values from the biexponential fit, unlike for dichloromethane guest [20], where the relaxation rates have similar values and data are obtained with high error.

From measured relaxation data, we can make following conclusion. When chloroform is free in the solution, its relaxation is clearly in the extreme narrowing regime, with the rate independent on the magnetic field and with full or almost full NOE. Motion of the free chloroform molecule is rather fast and non-restricted. The T_1 values for complexed chloroform are considerably shorter than those of the free one, they differ for the two magnetic fields and NOE factors are significantly less than full. Thus, the relaxation of the bound guest is outside of the extreme narrowing regime which indicates slower, restricted motion of the chloroform inside the cryptophane cavity. Moreover, T_1 and NOE values are very similar to the values of the host. This clearly indicates motional coupling of the host and the guest, i.e. the guest moves practically together with the host.

However, assumptions about the host and guest motion using measured values of relaxation times T_1 and NOE factors can be only qualitative. To obtain more complex picture of motions on different timescales, additional relaxation data for host molecule at different magnetic field and possibly for other host carbons should be measured. A motional model (e.g. Lipari-Szabo, truncated Lipari-Szabo) should be fitted to the measured data.

Chapter 7

Summary

This study was focused on investigation of cryptophane-C complex with chloroform in tetrachloroethane solvent. The formation of the inclusion complex between was documented by the appearance of the bound chloroform signal at 2.55 ppm in proton spectra, which was shifted upfield by 4.47 ppm from the signal of the free species. The spectra document slow chemical exchange between free and bound species at 400 and 600 MHz.

The kinetics of complex formation was determined by selective 1D NOESY experiments at four temperatures. According to these measurements, bound-to-free effective reaction rate is much higher than the opposite one, as a consequence of high free host concentration in comparison with the bound species. The equilibrium is shifted toward the free host and guest rather than toward the complex. The small abundance of the complex and low association equilibrium constant at used concentrations is a fact that has not been observed in previous studies of cryptophane inclusion complexes. [21, 22]

Measurements of carbon-13 longitudinal relaxation and heteronuclear Overhauser enhancement for chloroform molecule clearly show that the motion of the free host in the solvent is fairly isotropic, while chloroform stands rather firmly inside the cryptophane-C. The similarity of longitudinal relaxation rates and NOE enhancement factors for the guest and the host demonstrate full motional coupling between the host and the guest included in its cavity.

We attempted to determine whether there is a preferential chloroform orientation in the cavity due to the different substitution of the two cyclotriveratrylene units. Unfortunately, the performed ROESY experiments did not provide unequivocal results.

Part IV

Experimental Study of Molecular Clusters of Ethanol in Non-Polar Solvent

Chapter 8

Ethanol

8.1   General Properties

At normal conditions, ethanol is a liquid with density of 780 kg.m^{-3} with boiling point of 391 K and freezing point of 159 K. Chemical formula of ethanol is CH_3CH_2OH and molecular weight is 46.07 g.mol^{-1}.

Particularly low freezing and boiling temperature of ethanol (in comparison with molecules of similar molecular weight) is a consequence of hydrogen bonds connecting molecules of ethanol. Several molecules connected together with hydrogen bonds form a *molecular cluster*. Clusters are dynamic structures with varying size and very short life time.

8.2   Bibliography Review

Ethanol and its properties, either of neat ethanol or dissolved in water or non-polar solvents, have been studied for very long time using different experimental or theoretical approaches, which resulted in dozens of publications. Despite of that, the knowledge of cluster structures and formation dynamics is still fragmentary and even very recent published results are often inconsistent. At this point we chose to review only selected most relevant publications concerning investigation of clusters of ethanol.

Remarkable properties of hydrogen bond formation in liquids were investigated already since the beginning of the second half of 20th century. In one of the early works [24], water-ethanol mixtures were investigated by means of NMR spectroscopy and concentration dependence of chemical shift of OH protons was discovered. According to the results of this work, OH signal splits into two at a particular concentration of the ethanol, for which the mixture has also maximal viscosity.

Several other earlier works studied the hydroxyl proton chemical shifts in ethanol and possibly other alcohols. Among these studies, work of Saunders et al. [25] may be mentioned, where concentration dependence of the alcoholic hydrogen chemical shifts of several simple alcohols in CCl_4 has been measured in concentration region between 0.01 and 0.1 M (which is only slightly lower

than our samples, 0.16 and 1.4 M) at the temperature of 294 K. It was concluded that ethanol and methanol form an equilibrium mixture of monomers and tetramers at these conditions.

In several later studies, concerning ab initio calculations [26, 27, 28], cooperativity effect of the hydrogen bonding was investigated. It was shown, that the binding energies as well as intermolecular $O \cdots O$ distances decreases for bigger clusters of ethanol and also other low-molecular-weight alcohols. Due to the cooperativity effect, cyclic structures are said to be more stable than the linear ones and larger clusters are more favourable than the smaller ones. However, there is also entropy effect that makes very large clusters unfavourable.

Cooperativity effect is also discussed in the work of Hülsekopf et al. [29], where structures of ethanol clusters and their properties were calculated using QCE (Quantum Cluster Equilibrium) theory and the theoretical results were compared with experimental hydroxyl proton chemical shifts of neat ethanol in temperature range $250 - 350$ K. According to these data, it is claimed that cyclic tetramer and pentamer structures are the principal components of liquid ethanol.

According to the work of Ferris et al. [28], based on ab initio calculations, deuterium quadrupolar coupling measurements and OH proton chemical shift measurements on neat ethanol in temperature range from 280 to 340 K, the average cluster size is close to the cyclic pentamer and hexamer.

In the work of Murdoch et al. [30], infrared spectroscopy and ab initio calculated OH stretch frequencies were compared and according to these data, size of clusters and their population was estimated. The investigation was done on samples containing $0.45 - 4.0$ mol. % of ethanol (which is comparable to our sample with lower concentration, 2 mol. %) in non-polar solvent (hexane or CCl_4) at temperature range from 198 to 298 K. According to this work, the primary species present at room temperature is monomer with some small amount of linear dimer and trimer. At low temperature, the primary species present are cyclic pentamer and hexamer with small amount of cyclic tetramer.

Our results concerning cluster size are comparable to those obtained in works [30, 25], in which ethanol was studied at similar conditions than ours. However, it is necessary to notice that in most of the works in which neat ethanol or much higher concentrations of ethanol were investigated, the observed size of the clusters was larger or the same size as we observed in our work. This is at least questionable result concerning the concentration dependence of the cluster sizes.

Chapter 9

Experimental Section

9.1 Samples

Sample for HydroNMR calibration measurements was prepared in coaxial NMR tube set (Shigemi) with inner tube containing 1 vol. % TMS (99.9 %, NMR grade) dissolved in cca 400 μl of non-deuterated hexane and outer tube containing deuterated methanol for field-frequency lock (exact concentration of TMS is not important for our purposes). The reason for using non-deuterated hexane as a solvent is that its viscosity is tabulated while it is chemically identical to deuterated hexane.

For experimental measurements of ethanol, two samples with different concentration of ethanol were prepared. Pure ethanol (MERCK, absolute grade for analysis) was dissolved in deuterated hexane (99.0 % of deuterium guaranteed) and small amount of TMS standard was added into each sample. Amount of hexane was estimated using laboratory scales, the volume of ethanol was measured by Hamilton syringe. The samples were degassed by the freeze-pump-thaw procedure several times and flame-sealed in a 5 mm NMR tube. Molecular mass and density of hexane and ethanol used for calculation of sample concentration are in Table 9.1, resulting concentrations are in Table 9.2.

9.2 General

All NMR experiment were carried out with Bruker Avance spectrometer with resonance frequency for proton nuclei of 500 MHz (magnetic field of 11.7 T). For translational diffusion measurements on ^{1}H nuclei, TBO and TBI probes with gradient coils were used. Measured temperature range was $180-330$ K,

	density [kg.m^{-3}]	molecular weight [g.mol^{-1}]
ethanol	789	46.07
hexane-d$_{14}$	767	100.26

Table 9.1: Molecular weight and density of ethanol and deuterated hexane.

	1.4 M sample	0.16 M sample
hexane [g]	0.440	0.418
ethanol [μl]	50	5
vol. % of ethanol	8.0	0.9
mol. % of ethanol	16	2.0
molar concentration [M]	1.4	0.16

Table 9.2: Parameters of studied ethanol samples.

temperature calibration was done prior to the experiments using standard methanol sample (99.97 % of methanol + 0.03 % of HCl). Real sample temperature was calculated according to the formula

$$T = 403.0 - \frac{29.46}{\nu_0}|\Delta\nu| - \frac{23.832^2}{\nu_0}|\Delta\nu|^2, \tag{9.1}$$

where $\Delta\nu$ is the distance of methanol signals in Hz and ν_0 is the resonant frequency of ^{1}H nuclei.

Gradient power was calibrated according to measurement of known diffusion coefficient (0.1872×10^{-8} m^{2}s^{-1}) of doped water (D_2O + 1 % H_2O) at 298 K.

9.3 Experimental settings

Translational diffusion was measured on protons using double stimulated echo pulse sequence described in Section 3.3. Calibration TMS measurements and ethanol measurement at temperatures over 298 K were carried out with spin-lock, other ethanol measurements were carried out without spin-lock.

Number of scans was set to 16 + 2 dummy scans for TMS calibration measurements and to 8 without dummy scans for ethanol measurements. $\pi/2$-pulse length varied from 13.0 to 14.5 μs for the TBO probe and from 7.9 to 10.3 μs for the TBI probe over the measured temperature range. Diffusion mixing time settings can be seen in Table 9.3. For TMS calibration measurements, experiments were repeated twice at each temperature with the same settings.

Series of 1D spectra was recorded for 32 different values of gradient power, varying linearly from 2 to 100 % of full gradient power. Obtained decaying signal intensity was fitted to Gaussian decay according to the Equation 2.32. Example of intensity decay in dependence on changing gradient for 0.16 M ethanol sample at 307.9 K can be seen in Figure 9.1.

Diffusion coefficients were measured for all non-equivalent ^{1}H nuclei in each molecule separately (three for ethanol, two for hexane and one for TMS). The resulting diffusion coefficient for the molecule was taken as an average of these values. Examples of the diffusion spectra are in Figure 9.2.

T [K]		181.8	193.0	203.5	213.7	223.5	233.1
	TMS sample	100	80	60	50	50	40
t_{mix} [ms]	1.4 M sample	80	60	60	40	40	40
	0.16 M sample	80	80	60	40	40	40
T [K]		242.5	251.7	261.0	270.2	279.5	288.8
	TMS sample	50	30	10	25	20	20
t_{mix} [ms]	1.4 M sample	30	30	30	20	20	20
	0.16 M sample	40	30	20	20	20	20
T [K]		296.5	307.9	315.8	322.1	330.2	
	TMS sample	15	25	20	18	15	
t_{mix} [ms]	1.4 M sample	20					
	0.16 M sample	20	25	20	18	15	

Table 9.3: Settings of diffusion mixing time t_{mix} for calibration TMS measurements and ethanol measurements.
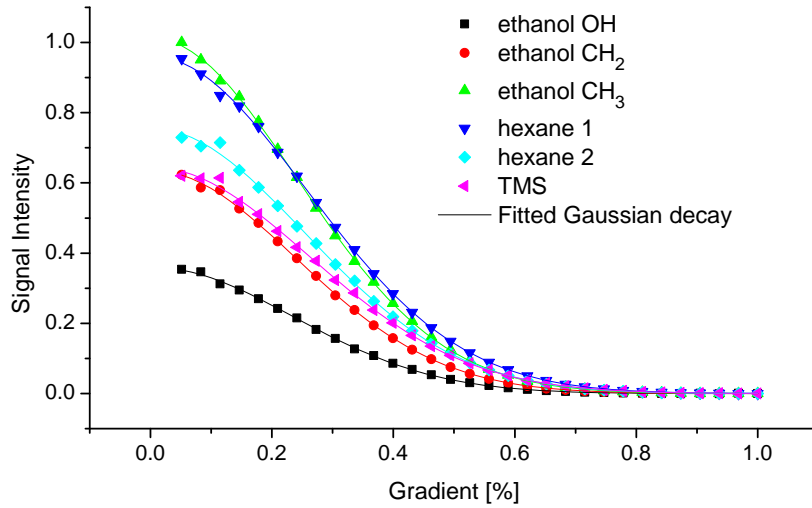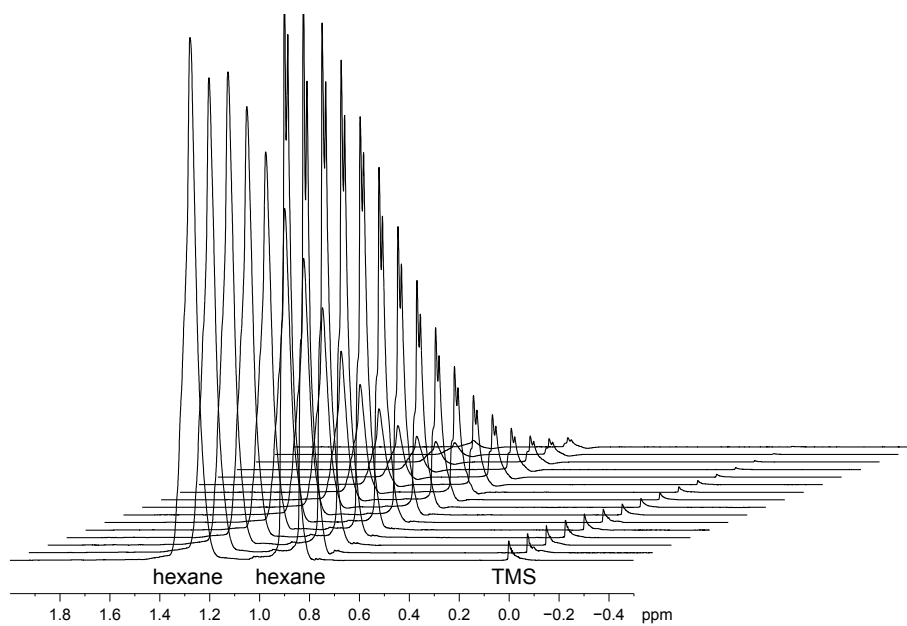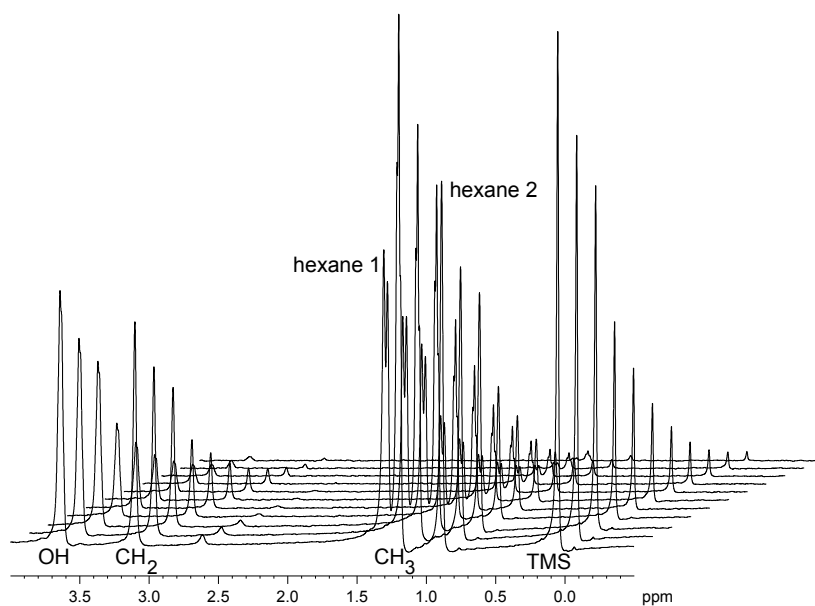

Figure 9.1: Gaussian decaying signal intensity of ethanol, deuterated hexane and TMS ^{1}H nuclei at 307.9 K, 0.16 M sample, diffusion mixing time 25 ms.

Figure 9.2: Diffusion spectra series for (A) TMS sample in non-deuterated hexane (B) and 0.16 M ethanol sample at 242.5 K.

Chapter 10

Results and Discussion

10.1 Hydroxyl Proton Chemical Shifts

In ^{1}H NMR spectra of ethanol, chemical shift of OH proton signal depends on temperature while chemical shifts of the CH_2 and CH_3 proton signals remain practically unchanged. This phenomenon is referred to be connected with the formation of the molecular clusters in the ethanol solution [24, 28, 29]. Hydroxyl proton involved in a hydrogen bond in a cluster experiences different environment depending on the size of cluster. Chemical shift measured at certain temperature is an population averaged value of all clusters present.

Measured hydroxyl proton chemical shifts δ_{OH} are presented in Table 10.1 and depicted in Graph 10.1. Series of spectra at different temperatures are presenting in Figure 10.2. Spectra were referenced according to the TMS signal.

The higher chemical shift means larger average size of the clusters. The temperature dependence varies for different concentrations, in more concentrated (1.4 M) sample, larger clusters are present than in the less concentrated one (0.16 M). Chemical shift decreases with temperature and, as can be seen for the 0.16 M sample, temperature course becomes saturated at high temperatures, where predominantly monomers are present.

T [K]		181.8	193.0	203.5	213.7	223.5	233.1
δ_{OH} [ppm]	0.16 M sample	6.30		6.11	6.00	5.87	5.72
	1.4 M sample	6.29	6.26	6.19	6.12	6.04	5.95
T [K]		242.5	251.7	261.0	270.2	279.5	288.8
δ_{OH} [ppm]	0.16 M sample	5.51	5.26	4.95	4.56	4.11	3.59
	1.4 M sample	5.84	5.74	5.61	5.45	5.29	5.08
T [K]		296.5	307.9	315.8	322.1	330.2	
δ_{OH} [ppm]	0.16 M sample	3.08	2.23	1.43	1.02	0.75	
	1.4 M sample	4.88					

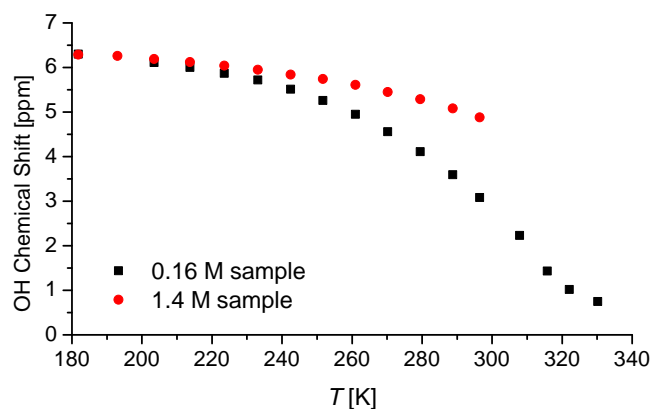Table 10.1: Measured hydroxyl proton chemical shift δ_{OH} for both 1.4 and 0.16 M sample.

Figure 10.1: Temperature dependence of hydroxyl proton chemical shift for both 1.4 and 0.16 M sample.
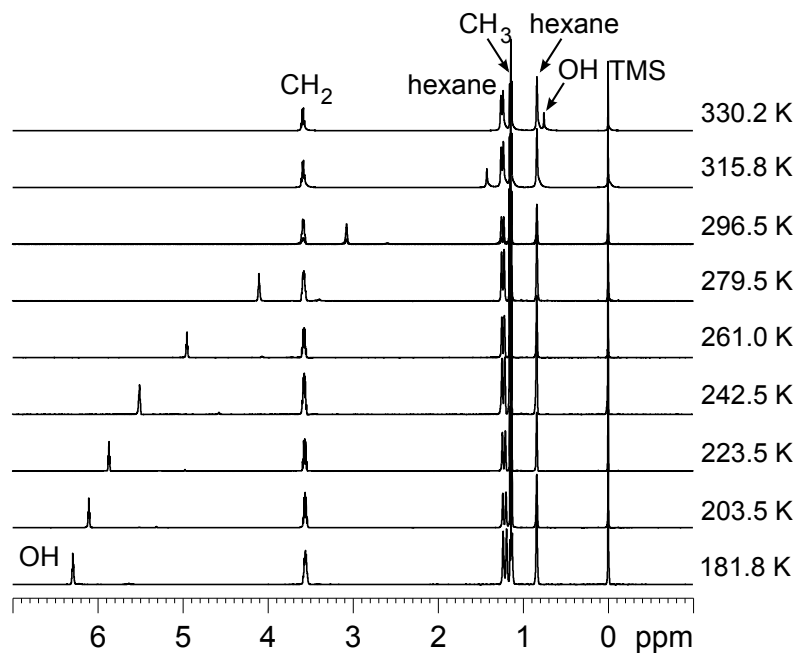

Figure 10.2: Temperature dependence of hydroxyl proton signal in ^{1}H spectra of 0.16 M sample.

10.2 Calibration Measurement of TMS in Hexane

HydroNMR is primarily intended for calculations of hydrodynamic properties of small rigid macromolecules. However, we took the challenge to test if it can be used also for calculation of translational diffusion coefficient of small molecules, or possibly molecular clusters.

10.2.1 Experimental Diffusion Coefficients of TMS

The input parameters, especially radius of the atomic elements a and radius of the minibeads σ, influences the construction of the bead model for particular molecule. To use the program for small molecules, one needs to verify correct setting of these parameters for these purposes. One way to do that is to calibrate these parameters according to the experimental values of translation diffusion coefficients for certain molecule. The input parameters should be adjusted in such a way, that the calculated diffusion coefficients correspond to the experimental ones.

For this purposes, we have chosen the molecule of tetramethylsilane, TMS. It has an advantage of being spherically symmetrical, which makes it suitable for hydrodynamic simulation as well as experimental diffusion measurements. TMS structure (see Figure 10.5 A) was obtained by DFT quantum chemical calculations.

NMR diffusion measurement were carried out in temperature range of $180-330$ K on a sample containing 1 vol. % of TMS in non-deuterated hexane.

Experimentally measured translational diffusion coefficients of TMS and hexane at different temperatures are presented in Figure 10.3.

Diffusion coefficients of hexane were not used in further calculations, we used them to verify the correctness of our measurements by comparison with published self-diffusion coefficients of hexane (Hariss, [31]). Grapf 10.4 shows perfect agreement of our data with the published results.

The coaxial tube system influenced the field homogeneity in the sample, which caused broadening of the feet of the peaks. TMS signal in the spectra was on the foot of the signal of hexane and was much smaller due to low concentration of TMS. All these problems causes difficulties with the processing of the spectra and additional errors in the resulting diffusion coefficient of TMS.

Experiments were repeated twice at each temperature. Statistical error based on Monte Carlo simulations of the fitted data was estimated as 2 %. This error seems to be underestimated, possibly due to occuring systematic error. Albeit it is not possible to evaluate the exact value of the systematic errors, they may increase the total experimental error up to 5-6 %.

10.2.2 Optimization of HydroNMR Input Parameters

In order to optimize HydroNMR input parameters, hydrodynamic simulations of TMS were carried out at the same conditions than the experiments.
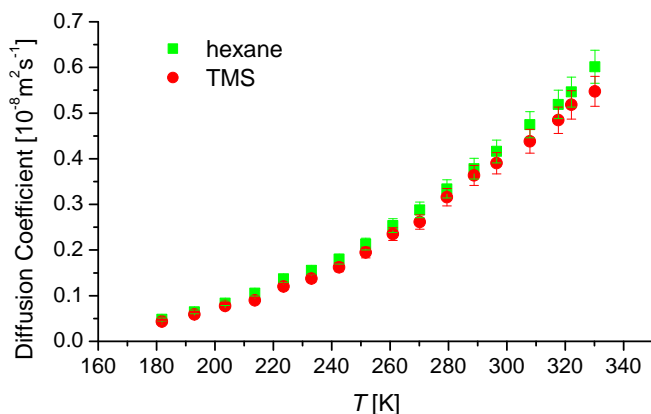
Figure 10.3: Experimental diffusion coefficients of TMS in hexane at different temperatures. Error bars show error of 6 %.
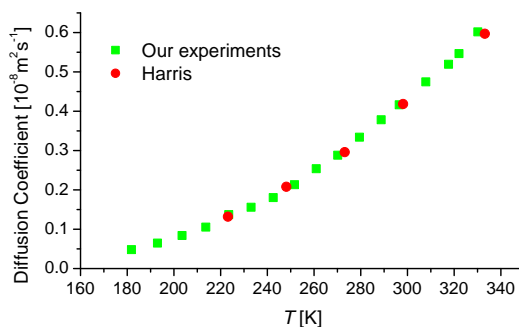

Figure 10.4: Comparison of diffusion coefficients of hexane with data published in Harris [31].

Viscosity of the non-deuterated hexane was taken from [32], fitted to an exponential of the 4th degree polynomial and interpolated to our temperature range (see Table 10.2).

Following the suggestions of the HydroNMR authors [10] (see Section 2.4.3), the parameter N_σ was set to 6, the value of σ_{min} was set such that the maximum number of minibeads was in range 1900-2000 and the value of σ_{max} such that the lowest amount of minibeads was between 400 and 500.

HydroNMR creates a primary hydrodynamic model according to the PDB file of TMS, consisting of 5 atomic spheres, as TMS contains 5 non-hydrogen atoms (see Figure 10.5 B). The radius of these atomic elements, a, should be optimized to arrive to the similar diffusion coefficient from the calculations and experiment.

Instead of comparing directly the diffusion coefficients, we chose rather to compare the product of diffusion coefficient and viscosity of the solvent
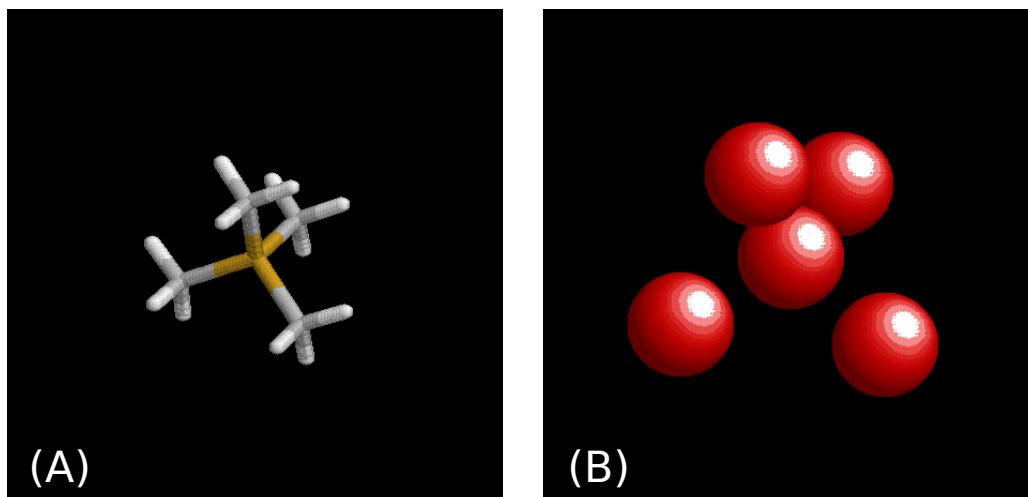
Figure 10.5: (A) Structure of TMS, (B) Primary hydrodynamic model for TMS, atomic spheres with $a = 0,73$ Å

(non-deuterated hexane), $D\eta$. This allowed us to get rid of the temperature dependence of viscosity. According to the Stokes-Einstein law (Eq. 2.24), the temperature dependence of $D\eta$ should be linear, which makes the comparison more convenient.

Error of the $D\eta$ can be considered as high as 6 %, coming from the error of D, which was discussed in the previous section. As we got rid of the exponential temperature dependence of D by multiplying it by viscosity, the dispersion of the $D\eta$ data (Graph 10.6 B) appears to be higher than the dispersion of the diffusion coefficients (Graph 10.6 A).

To eliminate the influence of dispersion of experimental $D\eta$, we have tried to match the calculated $D\eta$ to the linear fit to the experimental values. It turned out, that better correspondence of experimental and calculated values can be achieved if slightly temperature dependent values of a are chosen. Linear dependence $a(T)$ appeared to be satisfactory.

To find the best match, we tried to minimize the sum of the squared deviations $\sum \left[(D\eta)_{exp} - (D\eta)_{calc} \right]^2$ of the calculated data $(D\eta)_{calc}$ from the linear fit to the experimental data $(D\eta)_{exp}$. Due to the long HydroNMR computational time, we were not able to automatize this procedure and use a regular iterative methods.

The ad hoc procedure was chosen as follows: Firstly, we found the best a for the lowest and highest temperature (with the precision of 0.001 Å which is approx. 0.1 %). Then, we linearly interpolated these values for remaining temperatures, calculated diffusion coefficients, multiplied them by viscosity and calculated the sum of the squared deviations. By changing the values of a (in a steps of 0.001 Å) for the highest and lowest temperature around the firstly estimated values and repeating this procedure, we found $a(T)$ for which the sum of the squared residues was minimal. Results can be found in Figures 10.6 and 10.7 as well as in Table 10.2. These values were further used in

T	η	a	D_{exp}	D_{calc}
[K]	[10^{-4} Pa.s]	[Å]	[10^{-8} m^{2}s^{-1}]	[10^{-8} m^{2}s^{-1}]
181.8	18.96	0.730	0.043	0.039
193.0	13.89	0.738	0.059	0.057
203.5	10.86	0.746	0.077	0.077
213.7	8.83	0.754	0.090	0.098
223.5	7.41	0.762	0.120	0.122
233.1	6.36	0.770	0.138	0.148
242.5	5.55	0.778	0.162	0.175
251.7	4.90	0.785	0.195	0.204
261.0	4.37	0.793	0.235	0.236
270.2	3.93	0.801	0.261	0.270
279.5	3.56	0.809	0.316	0.307
288.8	3.23	0.817	0.363	0.346
296.5	3.00	0.825	0.390	0.381
307.9	2.71	0.832	0.438	0.434
317.6	2.49	0.840	0.484	0.485
322.1	2.40	0.844	0.518	0.508
330.2	2.24	0.851	0.548	0.556

Table 10.2: Experimental (D_{exp}) and calculated (D_{calc}) diffusion coefficients of TMS, η is the viscosity of non-deuterated hexane taken according to [32], a is the optimized radius of the atomic spheres.

the hydrodynamic simulation of ethanol molecular clusters, see Section 10.4.2.

The accuracy of HydroNMR calculated diffusion coefficients should be also mentioned. HydroNMR was tested several times with slightly varying minibead radii σ_{min} and σ_{max} and number of minibead radii used for extrapolation N_σ (but still within the suggested range) with other settings unchanged. Dispersion of obtained values was within 1 %. However, these test cannot evaluate errors caused by improper setting of parameters or inaccuracy of the hydrodynamic model itself.

## 10.3 Experimental Translational Diffusion Coefficients of Ethanol

10.3.1 Diffusion Coefficients

Translational diffusion coefficients were measured on two samples of ethanol dissolved in deuterated hexane. Experiments were carried out at temperature range $180-298$ K for the 1.4 M sample and at extended temperature range $180-330$ K for the 0.16 M sample.

Temperature dependence of diffusion coefficients for individual ^{1}H nuclei can be seen in Figure 10.8. The resulting diffusion coefficient for each molecule
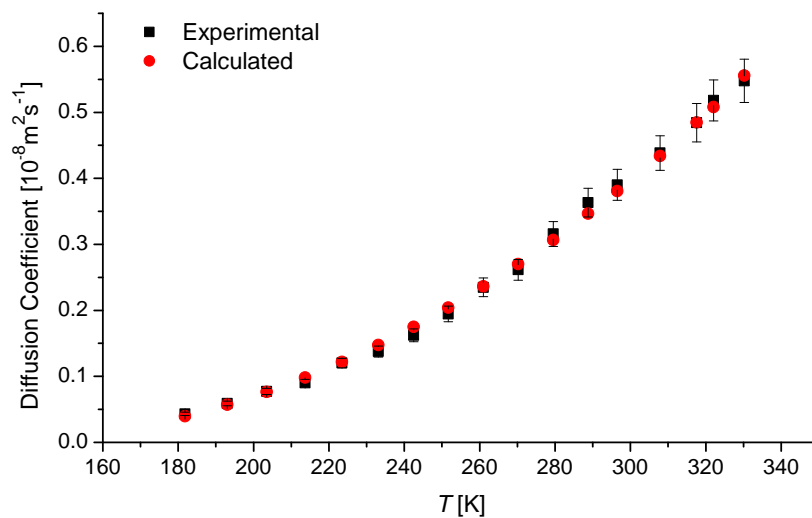
(A)
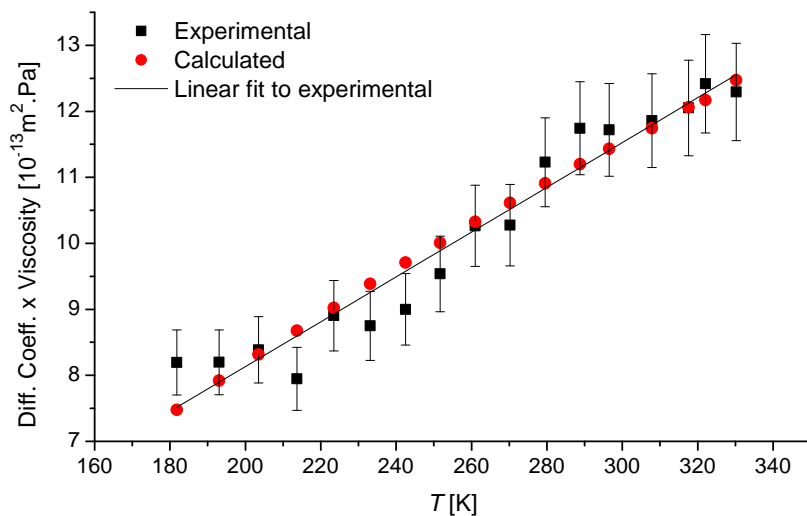
(B)

Figure 10.6: (A) Comparison of experimental and calculated TMS diffusion coefficients, (B) experimental $D\eta$ for TMS, linear fit to experimental data and HydroNMR calculated $D\eta$ for optimized $a(T)$. Error bars in both graphs show error of experimental data of 6 %.
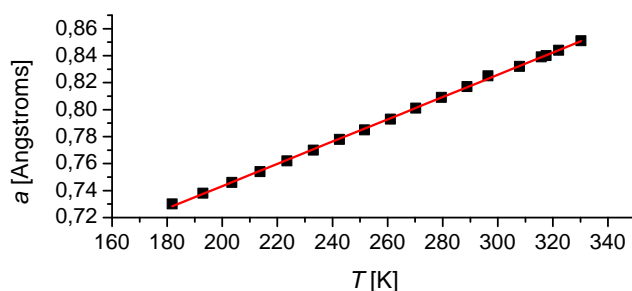
Figure 10.7: Temperature dependence of the optimized values of the radii of the atomic spheres a.

was taken as an average of all ^{1}H nuclei in the molecule (see Table 10.3 and 10.4).

Due to the better balanced intensity in the spectra and better separation of the peaks, the accuracy of measurements of ethanol samples is higher than the accuracy of the calibration TMS measurements. Error of diffusion coefficient obtained from Monte Carlo analysis ranges from 0.3 to 1 %. Diffusion coefficients of different signals in each molecule are also in good agreement. Exception is the signal of hexane in 1.4 M sample, which was influenced by the near signal of CH_3 ethanol group. This is not a significant problem, since diffusion coefficient of hexane is not important in further calculation. Taking into account that the real experimental error should be again considered slightly higher due to the possible systematic errors, reasonable estimate may be 4-5 %. For the sake of clarity, only errors for ethanol CH_2 and TMS data are depicted in graph in Figure 10.8.

As can be noticed from graphs in Figure 10.8, diffusion behaviour of ethanol molecules is different from the behaviour of hexane and TMS. Particularly for the 0.16 M sample, diffusion coefficient of ethanol is higher than the one of the hexane and TMS at temperatures over the room temperature. As the temperature decreases, the diffusion coefficient drops and for low temperatures is lower than the one of hexane and TMS.

This phenomenon can be considered as an indication of the presence of molecular clusters of ethanol, whose size is temperature dependent, within the sample. At room temperature, mostly monomers and small clusters are present, at lower temperatures the size of the clusters increases, therefore the diffusion coefficient decreases more rapidly. This is even more obvious, when we calculate the hydrodynamic radii of the molecules present.

10.3.2 Hydrodynamic Radii

Hydrodynamic radii of molecules present within the sample can be estimated according to the Equation 2.26, if the diffusion coefficient and viscosity of the solvent is known.

67
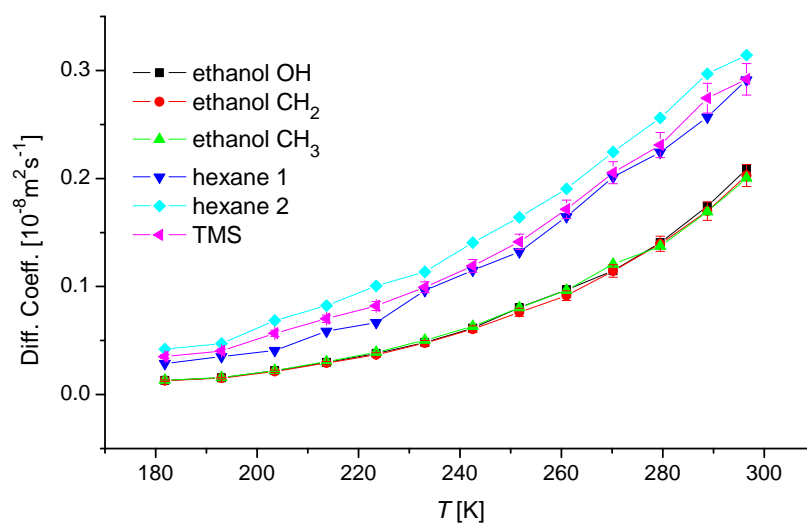
(A)
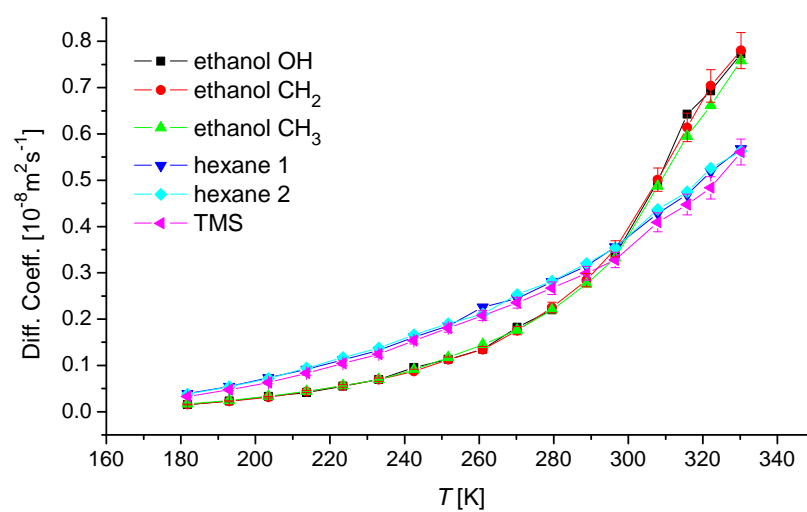
(B)

Figure 10.8: Temperature dependence of translational diffusion coefficient of ethanol in deuterated hexane for (A) 1.4 M sample and (B) 0.16 M sample. Error bars in both graphs show error of 5 %.

The viscosity of the deuterated hexane can be estimated by comparing the experimental diffusion coefficient of TMS in non-deuterated hexane and in deuterated hexane with ethanol. The comparison is based on assumption that the hydrodynamic radius of TMS in deuterated hexane is the same as in the non-deuterated hexane. This implies that the product of diffusion coefficient and viscosity of the solvent, $D\eta$, should be the same for both samples at each temperature. Therefore, viscosity of samples containing ethanol in deuterated hexane $\eta_{hex-d_{14}}$ can be calculated as

$$\eta_{hex-d_{14}} = \frac{D_{hex}^{TMS}\eta_{hex}}{D_{hex-d_{14}}^{TMS}} \qquad (10.1)$$

where η_{hex} is the viscosity of non-deuterated hexane, D_{hex}^{TMS} the diffusion coefficient taken according to the measurements of TMS in non-deuterated hexane (measured in order to calibrate HydroNMR input, see Table 10.2) and $D_{hex-d_{14}}^{TMS}$ is diffusion coefficient of TMS in deuterated hexane with ethanol (see Tables 10.3 and 10.4). It should be mentioned that rather than experimental values of $D_{hex}^{TMS}\eta_{hex}$ directly, we used the linear fit to these data (see Figure 10.6 A) for the viscosity calculation.

For resulting viscosity see Tables 10.3 and 10.4. The calculated viscosity slightly differs for the 1.4 and 0.16 M sample.

For results of hydrodynamic radii see Tables 10.3 and 10.4 and graph in Figure 10.9.

It should be point out that the hydrodynamic radii of TMS are the same for the two samples. Their values do not bring any new information, considering fact that the viscosity was calculated in such a way that TMS hydrodymanic radii in deuterated hexane are equal to the (smoothed by linear fit to $D\eta$) hydrodynamic radii of TMS in non-deuterated hexane.

Hydrodynamic radii accumulate experimental error from three sources: from the diffusion coefficient of the concerned molecule and from the viscosity of the deuterated hexane calculated according to the Equation 10.1 and thus from the diffusion coefficient of TMS both in non-deuterated and deuterated hexane. Due to this error propagation, hydrodynamic radii possess rather high error roughly estimated to 8 %. For the sake of clarity, only errors for ethanol are depicted in Graph 10.9.

Data presented in the graph in Figure 10.9 indicate that molecules of ethanol forms molecular clusters consisting of several molecules, whose size depends on temperature and concentration. With rising temperature, the size of the clusters decreases, from bigger clusters down to monomers at room temperature and at higher temperatures the decrease stops. Ethanol forms larger clusters in higher concentrated sample.

It is necessary to point out that diffusion measurements can provide us only the population average size of the clusters at each temperature.

To make these assumptions about the cluster sizes more quantitative, more elaborate approach is needed, as discussed further.

T [K]	η [10^{-4} Pa.s]	D [10^{-8} m^{2}s^{-1}]			r_H [Å]		
		ethanol	hexane	TMS	ethanol	hexane	TMS
181.8	21.24	0.013	0.035	0.035	4.8	1.8	1.8
193.0	19.53	0.015	0.041	0.040	4.7	1.8	1.8
203.5	14.54	0.022	0.055	0.057	4.7	1.9	1.8
213.7	12.25	0.030	0.071	0.070	4.3	1.8	1.8
223.5	10.88	0.038	0.084	0.082	4.0	1.8	1.8
233.1	9.32	0.049	0.105	0.099	3.8	1.7	1.8
242.5	8.05	0.062	0.128	0.119	3.6	1.7	1.9
251.7	7.01	0.079	0.148	0.141	3.3	1.8	1.9
261.0	5.96	0.095	0.177	0.172	3.4	1.8	1.9
270.2	5.14	0.117	0.213	0.205	3.3	1.8	1.9
279.5	4.71	0.139	0.240	0.231	3.1	1.8	1.9
288.8	4.08	0.171	0.277	0.274	3.0	1.9	1.9
296.5	3.93	0.204	0.303	0.292	2.7	1.8	1.9

Table 10.3: Experimental diffusion coefficients D and hydrodynamic radii r_H of ethanol, hexane and TMS for 1.4 M sample, η is the viscosity of deuterated hexane.

T [K]	η [10^{-4} Pa.s]	D [10^{-8} m^{2}s^{-1}]			r_H [Å]		
		ethanol	hexane	TMS	ethanol	hexane	TMS
181.8	22.98	0.016	0.039	0.033	3.6	1.5	1.8
193.0	16.60	0.023	0.054	0.048	3.7	1.6	1.8
203.5	13.09	0.033	0.072	0.063	3.5	1.6	1.8
213.7	10.34	0.043	0.093	0.083	3.5	1.6	1.8
223.5	8.55	0.056	0.114	0.104	3.4	1.7	1.8
233.1	7.47	0.069	0.135	0.124	3.3	1.7	1.8
242.5	6.23	0.091	0.164	0.154	3.1	1.7	1.9
251.7	5.47	0.114	0.188	0.181	3.0	1.8	1.9
261.0	4.91	0.138	0.219	0.208	2.8	1.8	1.9
270.2	4.47	0.178	0.249	0.235	2.5	1.8	1.9
279.5	4.06	0.222	0.281	0.267	2.3	1.8	1.9
288.8	3.73	0.280	0.317	0.299	2.0	1.8	1.9
296.5	3.48	0.341	0.355	0.328	1.8	1.8	1.9
307.9	2.88	0.495	0.433	0.409	1.6	1.8	1.9
315.8	2.70	0.617	0.472	0.447	1.4	1.8	1.9
322.1	2.54	0.686	0.522	0.484	1.4	1.8	1.9
330.2	2.24	0.770	0.565	0.561	1.4	1.9	1.9

Table 10.4: Experimental diffusion coefficients D and hydrodynamic radii r_H of ethanol, hexane and TMS for 0.16 M sample, η is the viscosity of deuterated hexane.
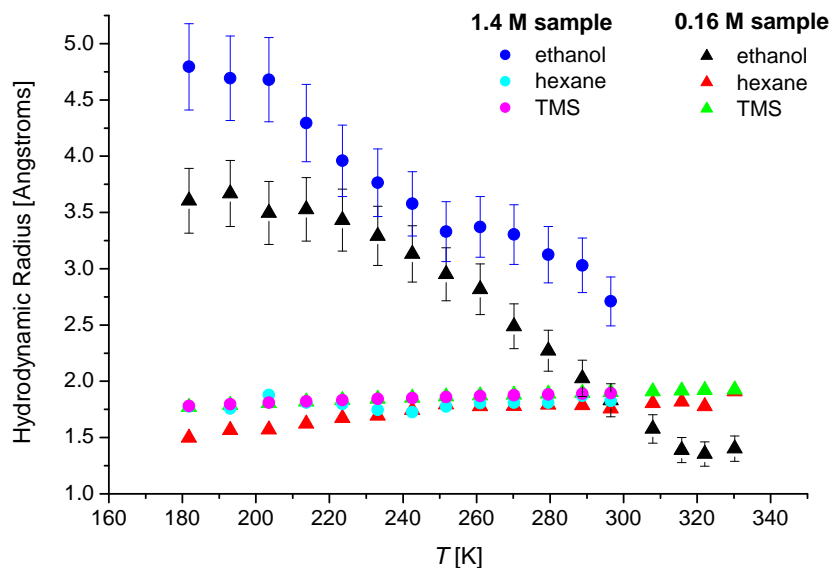
Figure 10.9: Temperature dependence of hydrodynamic radii of ethanol in deuterated hexane for both samples. Error bars show error of 8 %.

10.4 HydroNMR Simulation of Ethanol Clusters

Translation diffusion coefficients and hydrodynamic radii provide qualitative information about the formation of the molecular clusters, but not about the size of the clusters, i.e. the number of molecules contained within the cluster. For that purposes, we chose to compare diffusion coefficients of ab initio calculated structures of ethanol clusters with the experimental data, which allowed us to estimate how large the average clusters are.

10.4.1 Ab Initio Calculated Structures of Clusters

Ab initio structures of ethanol clusters were taken from previous work [3] dealing with theoretical calculations of hydrogen bond in ethanol solution. Structures were calculated using Density Functional Theory (DFT) method B3LYP. It was shown in this work that there are two possible conformations of ethanol molecule – *trans* and *gauche* (shown in Figure 10.10). Two types of clusters were considered – *linear*, in which connected molecules are in a line, and *cyclic*, where the first and the last molecule is connected with one more hydrogen bond.

We had at our disposal linear and cyclic structures from monomer (single ethanol molecule) up to octamer (containing eight molecules) consisting of either gauche or trans molecules (see Figures 10.11 – 10.13).

In hydrodynamic calculations, HydroNMR takes into account only non-
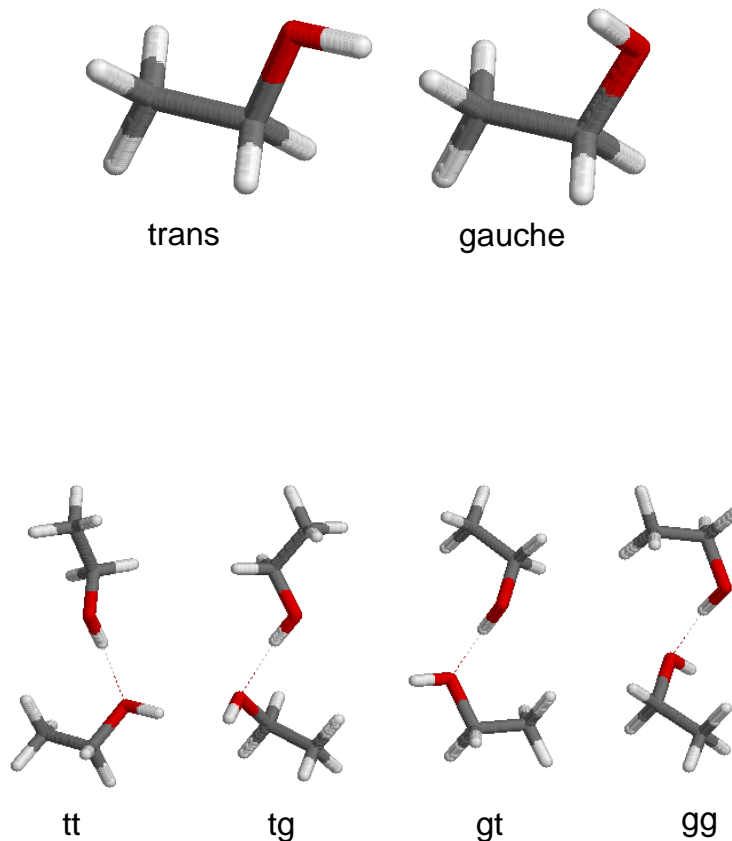
Figure 10.10: Monomers (single molecules) and dimers of ethanol molecules according to the DFT calculations in [3].

hydrogen atoms, i.e. primary hydrodynamic model contains three atomic spheres and does not differ for trans and gauche conformation of the molecule. Therefore, diffusion coefficient of clusters is expected to be very similar regardless of the conformation of molecules in the clusters. This was supported by diffusion calculation of cyclic clusters containing both trans and gauche molecules. According to this results, we do not further distinguish between trans and gauche conformation of the molecules.

10.4.2 Diffusion Simulations of Cluster Structures

Calculations were carried out separately for each chosen structure with conditions set equally to the experiments.

Viscosity of the solvent was taken according to the calculations in Section 10.3.2. As the viscosity for the two samples slightly differs (see Tables 10.3
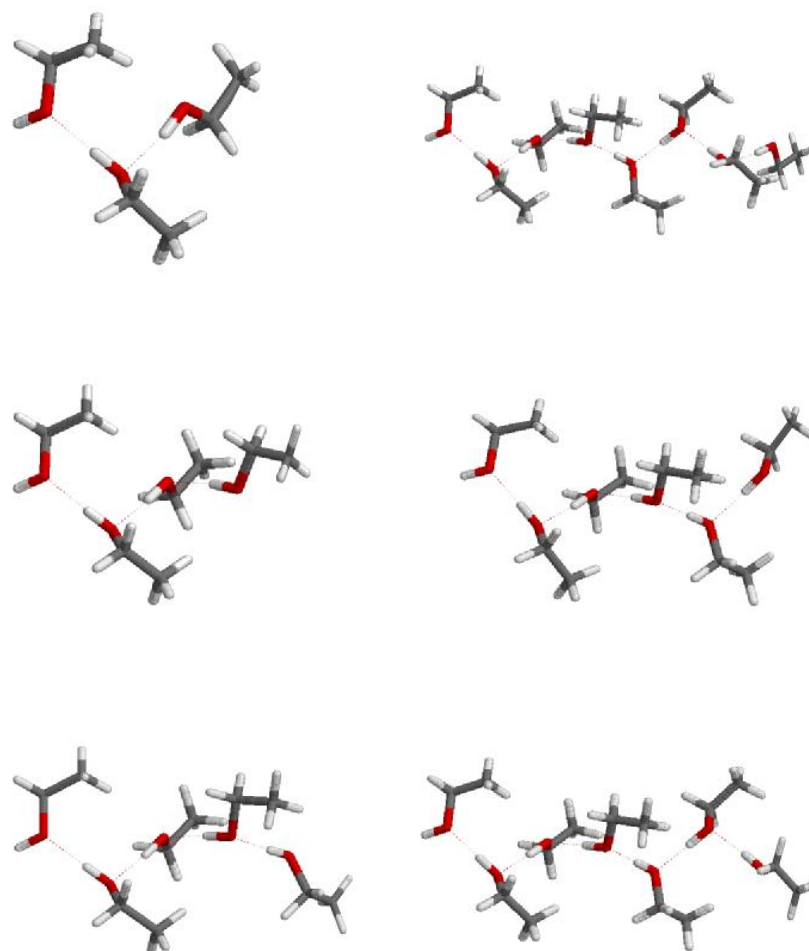
Figure 10.11: Linear trimer to octamer of ethanol consisting of trans molecules according to the DFT calculations in [3].
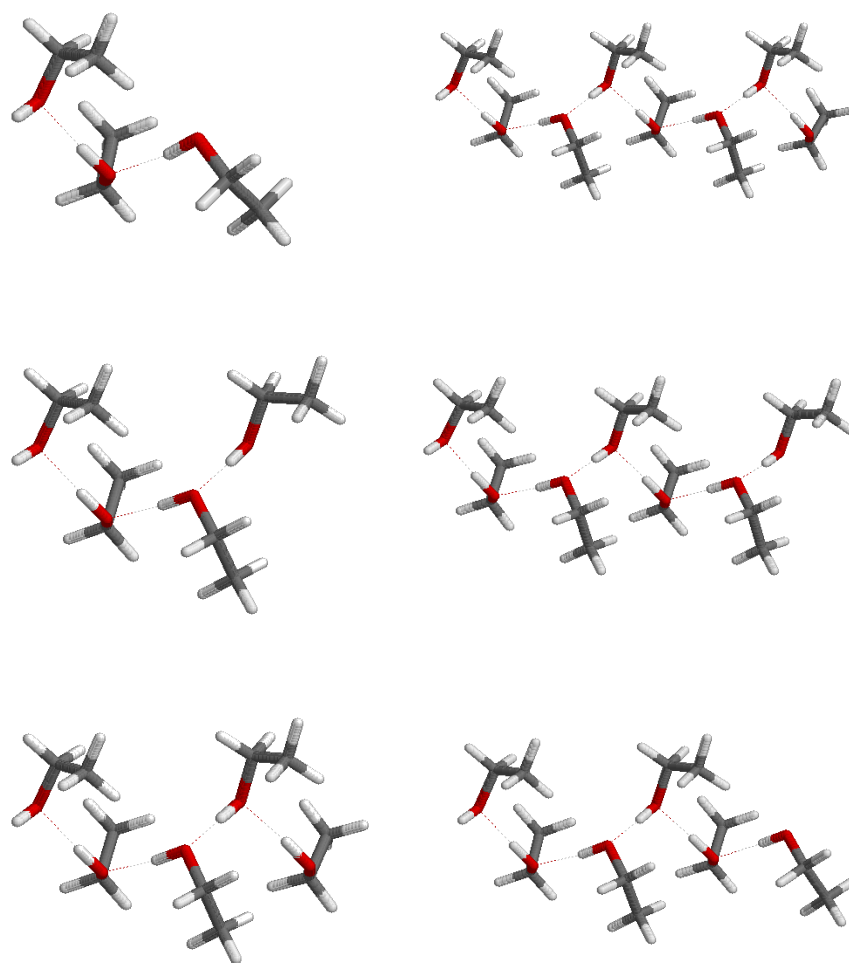
Figure 10.12: Linear trimer to octamer of ethanol consisting of gauche molecules according to the DFT calculations in [3].
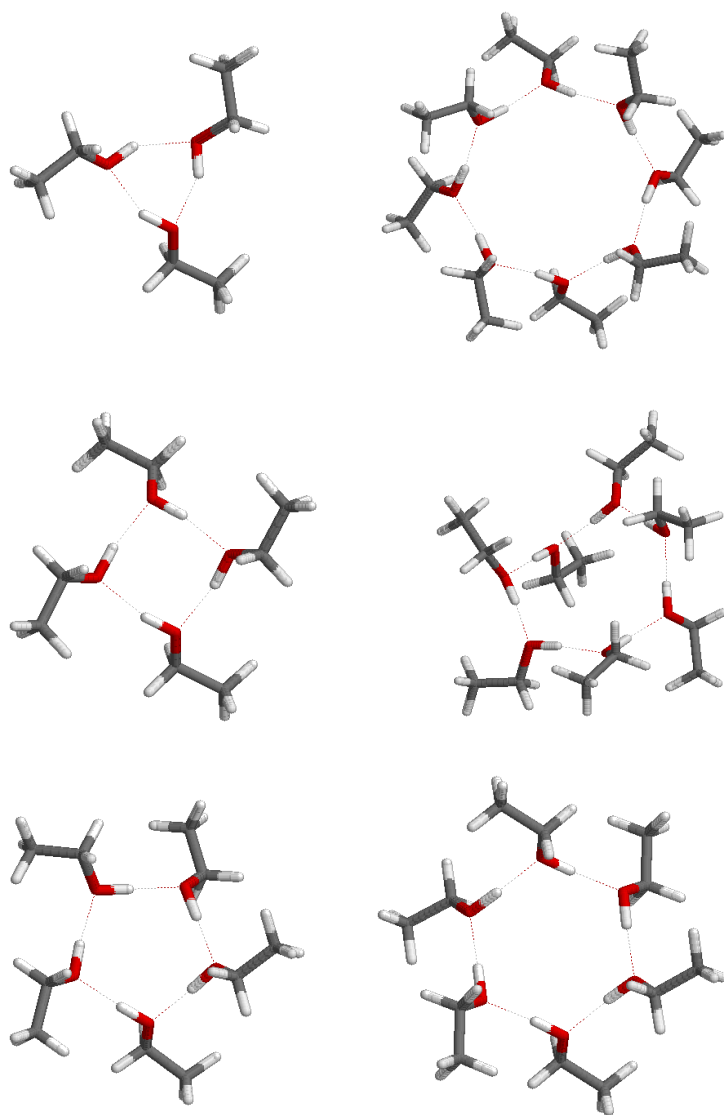
Figure 10.13: Cyclic trimer to octamer of ethanol consisting of trans molecules according to the DFT calculations in [3].
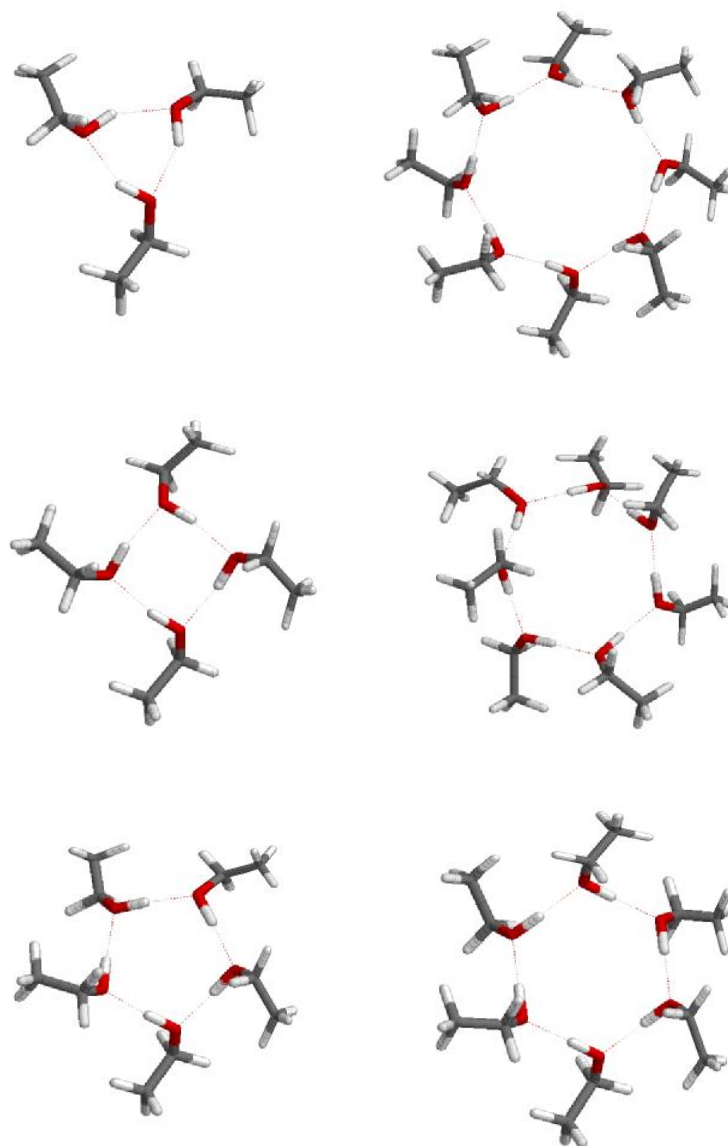
Figure 10.14: Cyclic trimer to octamer of ethanol consisting of gauche molecules according to the DFT calculations in [3].
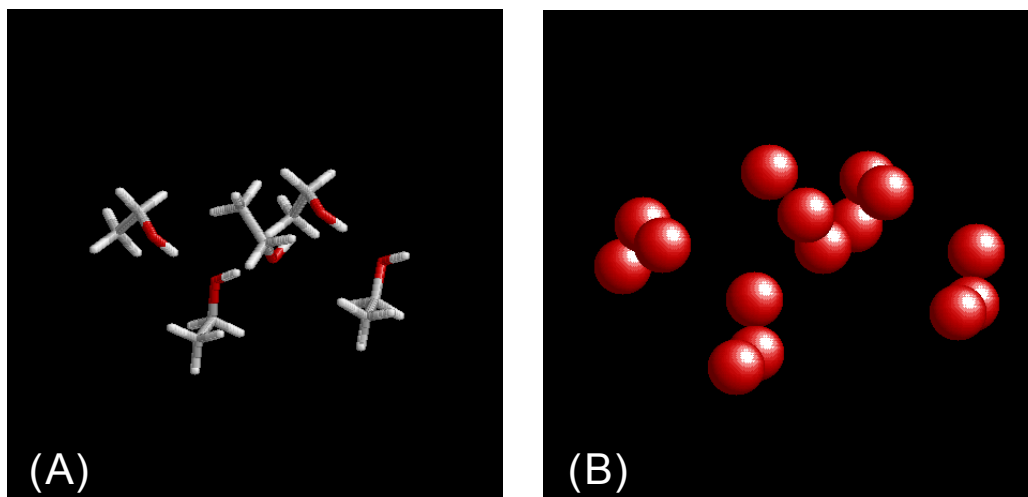
Figure 10.15: (A) Structure of linear pentamer, (B) Primary hydrodynamic model for linear pentamer, atomic spheres with $a = 0,73$ Å.

and 10.4), all the calculations were carried out twice with differently set viscosity. For the 0.16 M sample, both linear and cyclic structures were calculated, for the 1.4 M sample, only linear clusters were calculated. As can be seen in Figures 10.16 B and 10.17 B, diffusion behaviour of the linear and cyclic clusters differs very slightly. The difference between the hydrodynamic radii for linear and cyclic clusters is less than 2 %.

The radii of the atomic spheres for the primary hydrodynamic model were taken as calibrated due to TMS in hexane measurements (see Table 10.2). The settings of other parameters (minibead radii σ_{min} and σ_{max}, N_σ) were adjusted the same way as for the TMS simulations (see Section 2.4.3). Example of the primary hydrodynamic model for linear pentamer is depicted in Figure 10.15.

10.4.3 Average Size of Ethanol Molecular Clusters

HydroNMR calculated diffusion coefficient compared with experimental data for both 1.4 and 0.16 M ethanol samples are presented in Figure 10.16. Error of experimental data is 5 % as discussed in Section 10.3.1.

From the diffusion coefficients, hydrodynamic radii were further calculated using Equation 2.26 and results were again compared with experimental values for both samples, see graphs in Figure 10.17. Experimental error of experimental values of radii is 8 % as discussed in Section 10.3.2.

The comparison of calculated and experimental results gives us quantitative information about the population averaged size of clusters present within the samples. For 1.4 M sample, clusters with average size equal to trimer and tetramer are present at room temperature. For lower temperatures, cluster size increases to the size even larger than octamer.

Results obtained for the 0.16 M sample, for which also higher temperatures were measured, are even more interesting. This sample contains in general
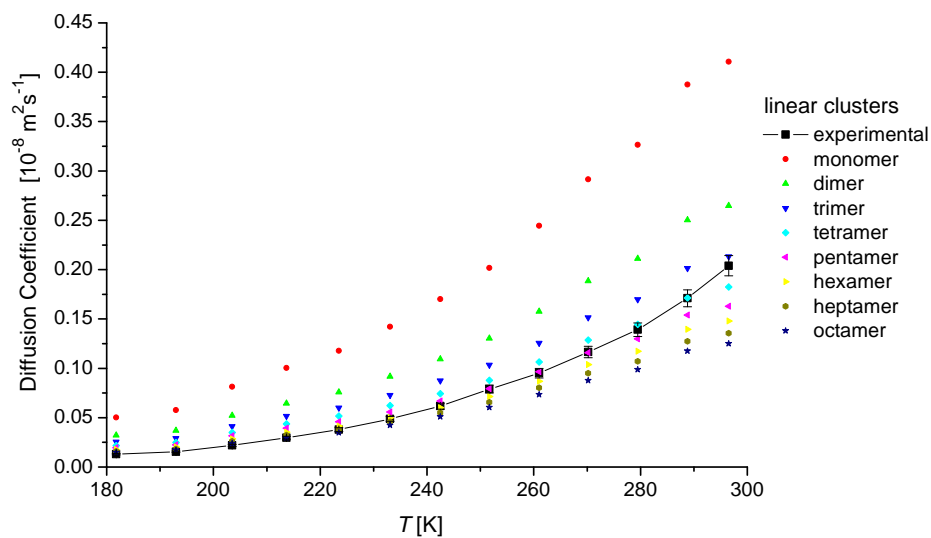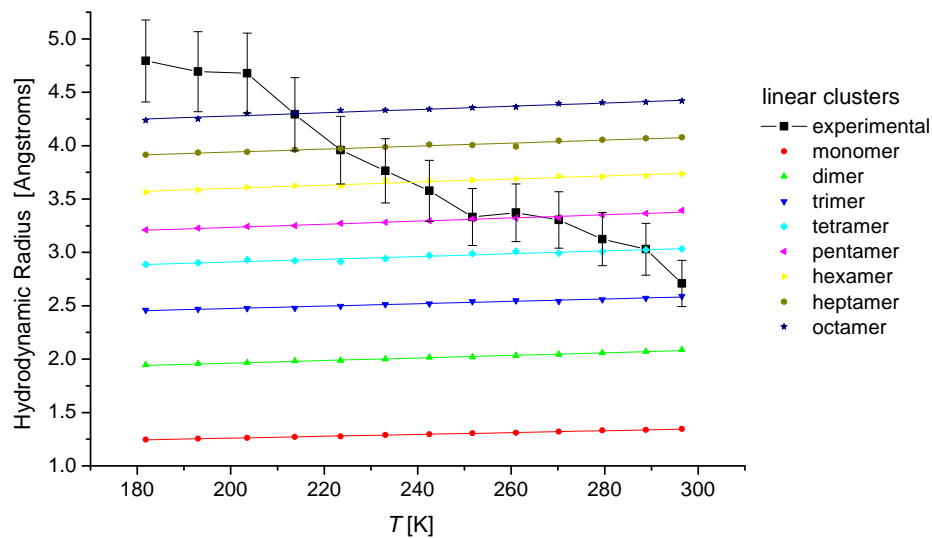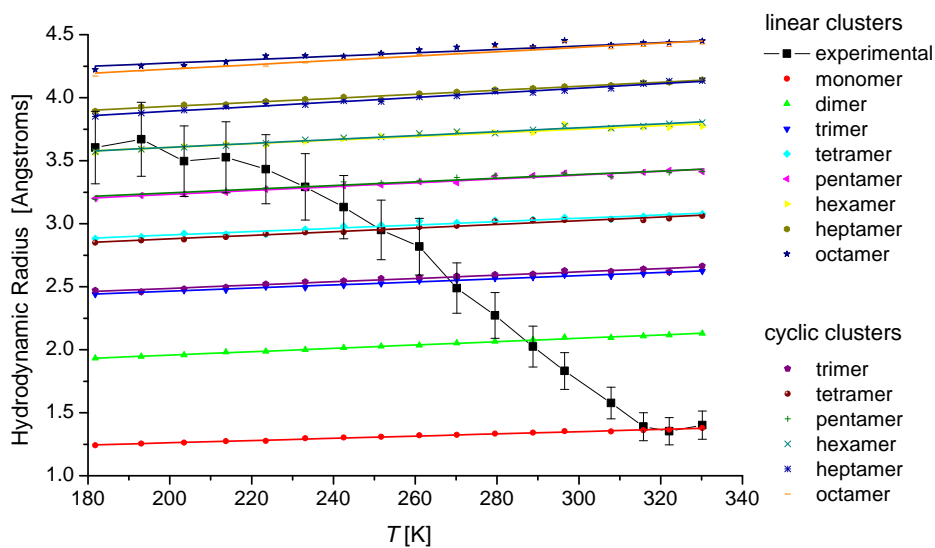
(A)
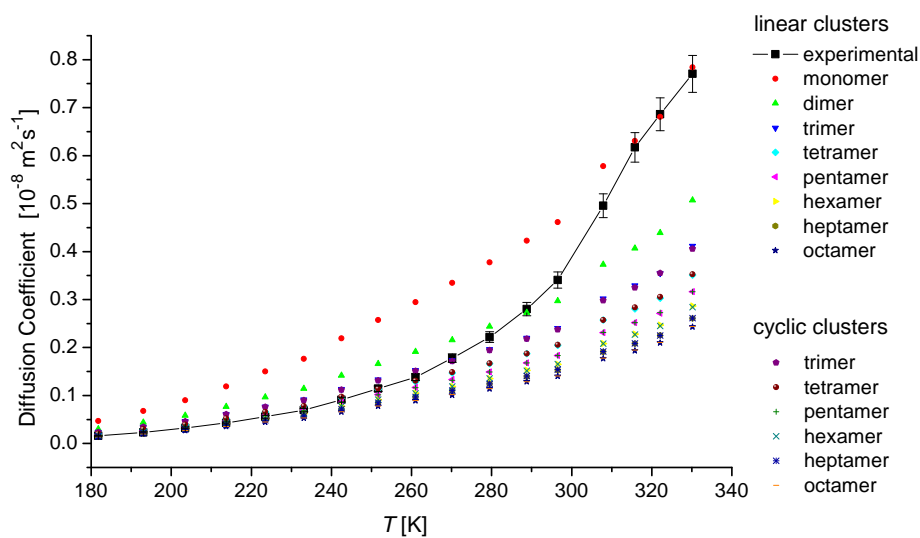
(B)

Figure 10.16: Comparison of experimental and calculated diffusion coefficients for (A) 1.4 M sample and (B) 0.16 mM sample. Error bars in both graphs show error of experimental data of 5 %.

(A)

(B)

Figure 10.17: Comparison of experimental and calculated hydrodynamic radii for (A) 1.4 M sample and (B) 0.16 mM sample. Error bars in both graphs show error of experimental data of 8 %.

smaller clusters than the more concentrated one at the same temperature. As can be seen from graph in Figure 10.17 B, hydrodynamic radius from experimental measurements decreases with the temperature up to approximately 308 K, where the decrease stops. That indicates that for higher temperatures than 308 K, only monomers are present in the sample and the radius does not decrease any more.

The temperature trend of hydrodynamic radii is in agreement with the trend of OH proton chemical shifts discussed in Section 10.1.

One can notice subtle temperature dependence of the hydrodynamic radii of cluster structures. This arises from the fact that slightly temperature dependent radii of the atomic spheres a were used for the hydrodynamic calculations. According to the calibration based on TMS measurements, this was necessary to achieve correspondence of calculated data with experimental results. This simply reflects the fact, that the behaviour of molecules in the samples is more complicated and does not strictly obey Stokes-Einstein low (on which the HydroNMR calculations are based).

Chapter 11

Summary

This study was focused on investigation of ethanol molecular clusters occurring in a solution with non-polar solvent. We combined experimental and theoretical approaches to obtain average size of the ethanol clusters in deuterated hexane in wide temperature range for two concentrations of ethanol.

We successfully applied HydroNMR program for calculation of diffusion coefficient of small molecules. For this purpose, we performed a calibration procedure consisting of comparison of calculated and experimental results for solution of TMS in hexane. The radius of atomic elements of HydroNMR primary model was adjusted to $0.730 - 0.851$ Å (lower than the value of 3.2 Å recommended for macromolecules). The applicability of HydroNMR on small molecules was confirmed by perfect agreement of the predicted and experimental hydrodynamic radius of monomeric ethanol.

Diffusion coefficients of ethanol solutions in deuterated hexane (0,16 M and 1.4 M) was measured in wide temperature range $180 - 330$ K. Using HydroNMR program with adjusted parameters, the diffusion coefficients of several types of clusters (linear or cyclic of different sizes, composed of molecules in gauche or trans conformations) were calculated. Only the size of the cluster was found significant for the resulting diffusion coefficient. The DFT optimized theoretical geometries of the clusters were taken from [3].

For the 1.4 M sample, the average size of the clusters present within the sample at low temperature (180 K) is even larger than octamer, at 298 K, the size of clusters approaches trimer. More interesting results are obtained for the 0.16 M ethanol sample. At low temperatures, the cluster size is approximately equal to hexamer. As the temperature increases, size of clusters reaches monomer at approximately 308 K and further remains the same.

Part V

Conclusion

11.1 Conclusion

Several NMR experimental methods were utilized in order to reveal nature of non-covalent binding in two selected supramolecular systems: inclusion complex of cryptophane-C with chloroform and molecular clusters of ethanol.

The host-guest complex of cryptophane-C and chloroform was studied from the complexation kinetics and NMR relaxation frame of reference. Kinetics of formation of the inclusion complex of cryptophane-C with chloroform was found rather slow in comparison with the complex decomposition. However, when chloroform is captured inside of the crytpophane cavity, there is full motional coupling between the host and the guest.

Novel methodology utilizing concerted use of NMR diffusion measurements and hydrodynamic calculations was used to determine the average size of the molecular clusters of ethanol. Applicability of our approach was verified by perfect agreement at high temperatures and low ethanol concentration where pure monomer occurs.

11.2 Future Work

It is certain that there are still many options how to improve and continue the investigation started in this work. The study of ethanol molecular clusters will continue by measurements carried out at higher temperatures for different concentrations of ethanol to achieve conditions, where monomers are present. The results will provide basis for investigation of clustering thermodynamics and will also be an important step from the average cluster sizes to the populations of clusters at measured temperatures. Furthermore, they will be employed for interpretation of nuclear spin relaxation measurements that have been impeded so far by inseparability of overall and internal molecular motions in ethanol.

Bibliography

[1] Brotin, T.; Dutasta, J. P.; Cryptophanes and Their Complexes - Present and Future *Chem. Rev.* **2009**, *109*, 88-130

[2] Hanyková, L.; Labuta, J,; Spěváček, J.; NMR Study of Temperature-Induced Phase Separation and Polymer-Solvent Interactions in Poly(Vinyl Methyl Ether)/D2O/Ethanol Solutions *Polymer* **2006**, *47*, 6107-6116

[3] Benda, L.; Computational Study on Structure and Properties of Ethanol Clusters, Diploma thesis at Department of Low Tmeperature Physics, Faculty of Mathematics and Physics, Charles University in Prague **2006**

[4] Englich J.; Pilař J.; Sedlák B.; Experimenální metody biofyziky II.; Státní pedagogické nakladatelství: Praha, 1983

[5] García de la Torre, J.; Huertas, M. L.; Carrasco, B.; HYDRONMR: Prediction of NMR Relaxation of Globular Proteins from Atomic-Level Structures and Hydrodynamic Calculations *J. Magn. Reson.* **2000**, *147*, 138-146

[6] Bloomfield, V. A.; Dalton, W. O.; Holde, K. E. V.; Frictional Coefficients of Multisubunit Structures. I. Theory *Biopolymers* **1967**, *5*, 135-148

[7] Bloomfield, V. A.; Dalton, W. O.; Holde, K. E. V.; Frictional Coefficients of Multisubunit Structures. II. Application to Proteins and Viruses *Biopolymers* **1967**, *5*, 149-159

[8] Carrasco, B.; García de la Torre, J.; Hydrodynamic Properties of Rigid Particles: Comparison of Different Modeling and Computational Procedures *Biophys. J.* **1999**, *75*, 3044-3057

[9] Bloomfield, V. A.; Filson, D. P.; Shell Model Calculations of Translational and Rotational Frictional Coefficients *J. Polym. Sci. Part C.* **1968**, *25*, 73-83

[10] User Guide to HydroNMR,

http://leonardo.fcu.um.es/macromol/programs/hydronmr/hydronmr.htm

[11] Kowalewski, J.; Mäler, L.; Nuclear Spin Relaxation in Liquids: Theory, Experiments, and Applications; Taylor & Francis Group: London, 2006

[12] Lipari, G.; Szabo, A.; Model-Free Approach to the Interpretation of Nuclear Magnetic Resonance Relaxation in Macromolecules. 1. Theory and Range of Validity *J. Am. Chem. Soc.* **1982**,*104*, 4546-4559

[13] Stejskal, E. O.; Tanner, J. E.; Spin Diffusion Measurements: Spin Echoes in the Presence of a Time-Dependent Field Gradient *J. Chem. Phys.* **1965**, *42*, 288-292

[14] Jerschow, A.; Müller, N.; Suppression of Convection Artifacts in Stimulated-Echo Diffusion Experiments. Double-Stimulated-Echo Experiments *J. Magn. Reson.* **1997**, *125*, 372-375

[15] Pelta, M. D.; Barjat, H.; Morris, G. A.; Davis, L. A.; Hammond, S. J.; Pulse Sequences for High-Resolution Diffusion-Ordered Spectroscopy (HR-DOSY) *Magn. Reson. Chem.* **1998**, *36*, 706-714

[16] Keeler, J.; Understanding NMR Spectroscopy; John Wiley & Sons: Chichester, 2005

[17] Stott, K.; Keeler, J.; Van, Q. N.; Shaka, A. J.; One-Dimensional NOE Experiments Using Pulsed Field Gradients *J. Magn. Reson.* **1997**, *125*, 302-324

[18] Collet, A.; Dutasta, J. P.; Lozach, B.; Canceill, J.; Cyclotriveratrylenes adn Cryptophanes: Theis Synthesis and Applications to Host-Guest Chemistry and to Designe New Materials *Top. Curr. Chem.* **1993**, *165*, 103-129

[19] Brotin, T.; Roy, V.; Dutasta, J.; Improved Synthesis of Functional CTVs and Cryptophanes Using Sc(OTf)3 as Catalyst *J. Org. Chem.* **2005**, *70*, 6187-6195

[20] Lang, J.; Dechter, J. J.; Effemey, M.; Kowalewski, J.; Dymanics of an Inclusion Complex of Chloroform and Cryptophane-E: Evidence for a Strongly Anisotropic van der Waals Bond *J. Am. Chem. Soc.* **2001**, *123*, 7852-7858

[21] Aski, S. N.; Lo, A. Y. H.; Brotin, T.; Dutasta, J. P.; Edén, M.;Kowalewski, J.; Studies of Inclusion Complexes of Dichloromethane in Cryptophanes by Exchange Kinetics ans ^{13}C NMR in Solution and the Solid State *J. Phys. Chem.*, **2008**, *112*, 13873-13881

[22] Aski, S. N; Takacs, Z.; Kowalewski, J.; Inclusion Complexes of Cryptophane-E with Dichloromethane and Chloroform: A Thermodynamics and Kinetic Study Using the 1D-EXSY Method *Magn. Reson. Chem.* **2008**, *46(12)*, 1135-1140

[23] Tošner, Z.; Lang, J.; Sandström, D; Petrov, O.;Kowalewski, J.; Dynamics of an Inclusion Complex of Dichloromethane and Cryptophane-E *J. Phys. Chem. A* **2002**, *106*, 8870-8875

[24] Ageno, M.; Indovina, P. L.; A Nuclear Magnetic Resonance Study of Water-Ethanol Mixtures *Proc. Natl. Acad. Sci. USA* **1967**, *5*, 1158-1163

[25] Saunders, M.; Hyne, J. B.; Study of Hydrogen Bonding in System of Hydroxylic Compounds in Carbon Tetrachloride through the Use of NMR *J. Chem. Phys.* **1958**, *29*, 1319

[26] Sum, A. K.; Sandler, I. S.; Ab Initio Calculations of Cooperativity Effects on Clusters of Methanol, Ethanol, 1-Propanol and Methanethiol *J. Phys. Chem* **2000**, *104*, 1121-1129

[27] Dynamics and Hydrogen Bonding in Liquid Ethanol *Mol. Phys.* **1999**, *97*, 897-905

[28] Ferris, T. D.; Farrar, T. C.; The Temperature Dependence of the Hydroxyl Deuterium Quadrupole Coupling Parameter and the Rotational Correlation Time of the OD Internuclear Vector in Neat Ethanol-d_1 *Mol. Phys.* **2002**, *100*, 303-309

[29] Hülsekopf, M.; Ludvig, R.; Temperature Dependence of Hydrogen Bonding in Alcohols *J. Mol. Liq.* **2000**, *85*, 105-125

[30] Murdoch, K. M.; Ferris, T. D.; Wright, J. C.; Farrar, T. C.; Infrared Spectroscopy of Ethanol Clusters in Ethanol-Hexane Binary Solution *J. Chem. Phys.* **2002**, *116*, 5717-5724

[31] Harris, K. R.; Temperature and Density Dependence of the Self-Diffusion Coefficient of n-Hexane from 223 to 333 K and up to 400 MPa *J. Chem. Soc.* **1982**, *78*, 2265-2274

[32] Giller, E. B.; Drickamer, H. G.; Viscosity of Normal Paraffins near the Freezing Point *Ind. Eng. Chem. Res.* **1949**, *41*, 2067-2069